HOMOGENIZATION OF NANOCOMPOSITES WITH AGGLOMERATING PARTICLES USING EMBEDDED ELEMENT METHOD

A THESIS SUBMITTED TO
THE GRADUATE SCHOOL OF NATURAL AND APPLIED SCIENCES
OF
MIDDLE EAST TECHNICAL UNIVERSITY

BY

ALPEREN DEMIRTAŞ

IN PARTIAL FULFILLMENT OF THE REQUIREMENTS
FOR
THE DEGREE OF MASTER OF SCIENCE
IN
AEROSPACE ENGINEERING

AUGUST 2023

Approval of the thesis:

HOMOGENIZATION OF NANOCOMPOSITES WITH AGGLOMERATING PARTICLES USING EMBEDDED ELEMENT METHOD

submitted by **ALPEREN DEMIRTAŞ** in partial fulfillment of the requirements for the degree of **Master of Science in Aerospace Engineering Department, Middle East Technical University** by,

Prof. Dr. Halil Kalıpçılar
Dean, Graduate School of **Natural and Applied Sciences** _____

Prof. Dr. Serkan Özgen
Head of Department, **Aerospace Engineering** _____

Assoc. Prof. Dr. Ercan Gürses
Supervisor, **Aerospace Engineering, METU** _____

Examining Committee Members:

Prof. Dr. Altan Kayran
Aerospace Engineering, METU _____

Assoc. Prof. Dr. Ercan Gürses
Aerospace Engineering, METU _____

Prof. Dr. Demirkan Çöker
Aerospace Engineering, METU _____

Assoc. Prof. Dr. Serdar Göktepe
Civil Engineering, METU _____

Assist. Prof. Dr. Ferit Sait
Aerospace Engineering, Atılım University _____

Date: 22.08.2023

I hereby declare that all information in this document has been obtained and presented in accordance with academic rules and ethical conduct. I also declare that, as required by these rules and conduct, I have fully cited and referenced all material and results that are not original to this work.

Name, Surname: Alperen Demirtaş

Signature :

ABSTRACT

HOMOGENIZATION OF NANOCOMPOSITES WITH AGGLOMERATING PARTICLES USING EMBEDDED ELEMENT METHOD

Demirtaş, Alperen
M.S., Department of Aerospace Engineering
Supervisor: Assoc. Prof. Dr. Ercan Gürses

August 2023, 79 pages

Composite materials are used in different industries due to their superior and tunable properties. On the other hand, analytical approaches and tests are challenging and insufficient in the computation of their mechanical properties. Therefore, precise and efficient procedures should be used to calculate their homogenized effective properties.

The aim of this study is to create a framework to compute the effective mechanical properties of nanocomposites efficiently and precisely. A crucial point to consider while calculating the effective properties is the effect of agglomeration. The agglomeration generally negatively affects the mechanical properties of nanocomposites.

While achieving the objective, various methods are employed, and scripts are written to ease the computational process. Using representative volume elements and employing the embedded element method ease the preprocessing effort and the computational cost. Numerous studies have been conducted to prove the efficiency and reliability of the methods. After proving that the aforementioned approaches give com-

patible results after convergence studies, the outcomes of the studies are presented. Agglomerations are formed as larger spheres inside the matrix. Close particles vanish, and agglomeration is placed instead of selected particles. The mechanical properties of the agglomeration are assigned using the inverse rule of mixture. The effect of the agglomerations is observed by comparing the homogenized elastic properties of cases with and without agglomerations using the computational homogenization method. Also, a study is conducted showing the relation between the particle size and agglomeration effect on mechanical properties. Ultimately, the results are compared with the literature, and similar trends in the degradation of elastic properties are observed.

Keywords: Nanocomposite, Homogenization, Agglomeration, Embedded Element Method, Representative Volume Element

ÖZ

TOPAKLANABİLİR KATKI İÇEREN NANOKOMPOZİTLERİN GÖMÜLÜ ELEMAN YÖNTEMİYLE HOMOJENLEŞTİRİLMESİ

Demirtaş, Alperen
Yüksek Lisans, Havacılık ve Uzay Mühendisliği Bölümü
Tez Yöneticisi: Doç. Dr. Ercan Gürses

Ağustos 2023 , 79 sayfa

Kompozit malzemeler üstün ve ayarlanabilir özelliklerinden dolayı farklı endüstrilerde kullanılmaktadır. Öte yandan analitik yaklaşımlar ve testler mekanik özelliklerinin hesaplanmasında zorlu ve yetersizdir. Bu nedenle homojenleştirilmiş etkin özellikleri hesaplamak için kesin ve etkili prosedürler kullanılmalıdır.

Bu çalışmanın amacı nanokompozitlerin etkin mekanik özelliklerini verimli ve hassas bir şekilde hesaplamak için bir çerçeve oluşturmaktır. Etkin özellikleri hesaplarken dikkate alınması gereken önemli bir nokta, topaklanma etkisidir. Topaklanmanın genellikle nanokompozitlerin mekanik özelliklerine negatif yönde bir etkisi olur.

Amaca ulaşırken çeşitli yöntemler kullanılmakta ve hesaplama sürecini kolaylaştırmak için algoritmalar yazılmaktadır. Temsili hacim elemanlarının kullanılması ve gömülü eleman yönteminin kullanılması, modelleme çabasını ve hesaplama maliyetini azaltır. Yöntemlerin etkinliğini ve güvenilirliğini kanıtlamak için çok sayıda çalışma yapılmıştır. Söz konusu yaklaşımların yakınsama çalışmaları sonrasında uyumlu so-

nuçlar verdiği kanıtlandıktan sonra çalışmaların sonuçları sunulmaktadır. Topaklanmalar matrisin içinde daha büyük küreler halinde oluşturulur. Birbirine yakın parçacıklar kaldırılır ve seçilen parçacıkların yerine topaklanmalar yerleştirilir. Topaklanmanın mekanik özellikleri ters karışım kuralı kullanılarak belirlenir. Topaklanmaların etkisi, hesaplamalı homojenleştirme yöntemi kullanılarak topaklanan ve topaklanmayan vakaların homojenleştirilmiş elastik özelliklerinin karşılaştırılması yoluyla gözlemlenir. Ayrıca parçacık boyutu ile topaklanmaların mekanik özellikler üzerindeki etkisini gösteren bir çalışma yapılmıştır. Son olarak sonuçlar literatürle karşılaştırılmış ve elastik özellikler üzerinde benzer negatif eğilimler gözlemlenmiştir.

Anahtar Kelimeler: Nanokompozit, Homojenleştirme, Topaklanma, Gömülü Eleman Yöntemi, Temsili Hacim Elemanı

To my honorable father, Alişen Demirtaş

ACKNOWLEDGMENTS

Foremost, I would like to express my deepest and sincere gratitude to my mentor, supervisor, Assoc. Prof. Dr. Ercan Gürses for his endless patience, guidance, encouragement, and criticism throughout this research.

I would like to thank the thesis committee members, Prof. Dr. Altay Kayran, Prof. Dr. Demirkan Çöker, Assoc. Prof. Dr. Serdar Göktepe and Asst. Prof. Dr. Ferit Sait for their interest and participation.

I would like to thank my friend Musa Batır, who supported and encouraged me throughout this study.

I also would like to thank my friends Yaren Sıla Özyalçın and Safa Yılmaz for their presence and support.

Finally, I would like to express my gratitude to my parents and my brother for their endless love and support.

TABLE OF CONTENTS

ABSTRACT v

ÖZ vii

ACKNOWLEDGMENTS x

TABLE OF CONTENTS xi

LIST OF TABLES xiii

LIST OF FIGURES xiv

LIST OF ABBREVIATIONS xvii

CHAPTERS

1 INTRODUCTION 1

1.1 Overview 1

1.2 Motivation and Aim of Thesis 3

1.3 Scope and Roadmap of Thesis 4

2 HOMOGENIZATION OF NANOCOMPOSITES 7

2.1 Homogenization Methods 8

2.2 Embedded Element Method 11

2.3 Agglomeration 14

3 METHOD OF APPROACH 21

3.1 Homogenization Method 21

3.1.1 Finite Element Model of the RVE 26
3.1.2 Random Sequential Adsorption Algorithm 27
3.1.3 Representative Volume Element 28
3.1.4 Boundary Condition 29
3.2 Formation of the Agglomeration 34
3.3 Embedded Element Method 37
4 NUMERICAL RESULTS 41
4.1 Convergence with Mesh Size 41
4.2 Convergence with Number of Particles 44
4.3 Comparison of EEM and FEM Results 46
4.4 Comparison of Different Boundary Conditions 48
4.5 Homogenized Elastic Constants 50
4.6 Comparison with Experiments 51
5 CONCLUSION 57
REFERENCES 61
A 69
B 71
C 79

LIST OF TABLES

TABLES

Table 2.1 Comparison of the numerical and Digimat results for the cases [32] . 13

Table 4.1 Homogenized elastic modulus results of various mesh densities . . . 43

Table 4.2 Homogenized elastic modulus results of the five cases of the study of the convergence of the number of particles 44

Table 4.3 Homogenized elastic modulus results of FEM and EEM 47

Table 4.4 Average elastic modulus results of the RVEs with single inclusion and multi-inclusion 47

Table 4.5 Comparison of homogenized elastic constants results with DBC and PBC 50

Table 4.6 Homogenized elastic modulus results of the nanocomposite 50

Table 4.7 Homogenized shear modulus results of the nanocomposite 51

Table 4.8 Variation of the cluster numbers with volume fractions and critical distance 53

Table A.1 Comparison of the cases with and without correction 70

LIST OF FIGURES

FIGURES

Figure 1.1 The illustration of the agglomeration formation relation with the aspect ratio of the carbon nanotubes [60] 3

Figure 2.1 The illustration of the homogenization. The honeycomb structure is also used in the sandwich composites 7

Figure 2.2 Illustrations of the models of Voigt and Reuss [30] 8

Figure 2.3 Comparison of the analytical homogenization techniques 10

Figure 2.4 Illustrations of (a) single unidirectional fiber, (b) irregularly distributed unidirectional fiber, (c) a single crimped yarn, (d) 5H satin-reinforced composite models [53] 12

Figure 2.5 RVEs of; (a) Case a: aligned fibers with 30% volume fraction, and (b) Case b: randomly dispersed shot carbon fibers with 10% volume fraction [32] 13

Figure 2.6 Transmission electron microscopy (TEM) image of (a) 50 nm gold particles, (b) 250 nm gold particles, (c) Example of a 250 nm gold particle. The bar length is 100 nm [14] 14

Figure 2.7 Comparison of the numerical, experimental, and analytical results of CNC/PA6 nanocomposite [8] 16

Figure 2.8 Comparison of the numerical and experimental results grafted and non-grafted particles for the cases with and without agglomerations [3] 17

Figure 2.9 Illustrations of agglomerations: (a) TEM image [15], (b) molecular dynamics model, and (c) finite element model [50] 18

Figure 2.10 (a) Illustration of the placements of the particles and (b) the illustration of the resin-free area [11] 19

Figure 3.1 An illustration of the domain divided into small pieces in the size of the particles 27

Figure 3.2 An RVE Sample from a Composite Component [39] 28

Figure 3.3 Illustration of the RVE with randomly distributed spherical inclusions with a 15% volume fraction. The surfaces, corner nodes, and edges are named using directions: east, west, north, south, top, and bottom [41] 32

Figure 3.4 Illustration of the periodic boundary condition applied deformed rectangular two-dimensional RVE [6] 33

Figure 3.5 Applied displacement boundary conditions. Uniaxial tensile tests in (a) x-direction, (b) y-direction, (c) z-direction, and shear tests in (d) xy-plane, (e) xz-plane, and (f) yz-plane 34

Figure 3.6 Illustration of the critical distance between randomly dispersed particles. The minimum value of the critical distance is $2r$ 35

Figure 3.7 Illustration of agglomeration formation without control script . . 36

Figure 3.8 Illustration of agglomeration formation with control script 36

Figure 3.9 (a) Schematic of the constraint between embedded and host nodes, (b) illustration of the multi-carbon nanotube model [34] 37

Figure 3.10 Illustrations of the embedded and host regions in a single inclusion RVE 38

Figure 3.11 Flowchart for the computation of the homogenized mechanical properties 39

Figure 4.1 Results of the mesh convergence study of a single inclusion RVE with 6.5% volume fraction 42

Figure 4.2 Illustration of the final discretization of a single inclusion RVE according to the results 43

Figure 4.3 Results of the convergence of the number of particles study to observe the agglomeration effect with 5% volume fraction. The number of inclusions axis is on a logarithmic scale. 45

Figure 4.4 Illustrations of the RVEs with (a) well-dispersed and (b) agglomerating particles for 125 numbers of particles with radius 0.25nm. 46

Figure 4.5 Illustrations of the application of (a) periodic boundary conditions and (b) linear displacement boundary conditions 49

Figure 4.6 Illustrations of deformed RVEs with (a) periodic boundary conditions and (b) displacement boundary conditions applied under shear load 49

Figure 4.7 Comparison of the results of the present study with the experiment 52

Figure 4.8 Comparison of the results with experiment with 12nm particle size while $\delta_{cr} = 4r$ 54

Figure 4.9 Comparison of the results with experiment with 20nm particle size while $\delta_{cr} = 3.2r$ 55

Figure 4.10 Comparison of the results with experiment with 40nm particle size while $\delta_{cr} = 2r$ 55

LIST OF ABBREVIATIONS

DBC	Displacement Boundary Condition
DOF	Degree of Freedom
EEM	Embedded Element Method
FEM	Finite Element Method
IVOL	Integration Point Volume
PBC	Periodic Boundary Condition
ROM	Rule of Mixture
RSA	Random Sequential Adsorption
RVE	Representative Volume Element

CHAPTER 1

INTRODUCTION

1.1 Overview

Composites are materials that are widely used in various industries such as defense, aviation, electronics, and automotive due to their superior properties, such as their lightweight and high strength. One major advantage of composite materials is their tunable mechanical properties. The purpose of composites usage can vary for each industry due to their adjustable properties.

Composite materials consist of at least two different materials: matrix and reinforcements. The matrix can be thermoset/thermoplastic polymers, ceramic or metallic material. In some applications, more than one reinforcement material can be included. Subcomponents of the composite materials provide different advantages to the system, such as while the matrix provides lightweight; reinforcement materials increase stiffness. These reinforcement materials can be in different shapes, such as spherical, sheets, rod-like or fiber-like, conical, or arbitrary shapes. The geometries of the reinforcements affect the mechanical properties of the overall composite material. For example, in fiber-like or rod-like geometries where all fibers are aligned, the elastic modulus of the whole composite material in longitudinal, i.e., fiber, direction increases.

The only benefit of using composite material is not increasing stiffness while decreasing the weight of a structure. Also, the composite material's permeability, thermal conductivity, opacity, and electrical conductivity can be tuned by varying matrix and reinforcement materials. Additionally, the components' volume and mass frac-

tions also change the overall system's properties. Therefore, there is always one or more optimum design points when it comes to composite materials.

According to [10], composite materials divide into three major groups: fiber-reinforced composites, particulate composites, and laminated composites. Besides the aforementioned conventional types of composites, nanocomposites are also used in practice, which include nano-sized fillers.

The most common matrix material in nanocomposites is polymers, and inclusions can be divided into three types: fibers, platelets, and particles [25]. Nanoinclusions can be carbon-based, metal, ceramics, semiconductor, and polymers [27].There are many kinds of nanofibers that are used in literature, such as chopped fibers, short metal, metal-coated fibers, mineral fibers, and the single crystal short fibers called whiskers [35]. Generally, slender fibers are used in practice with a high aspect ratio (from 10 to 100) [10]. The aspect ratio is the ratio of the length to the diameter of the fiber. The elastic modulus of the carbon nanotube, which is one of the common materials in practice, can reach up to 1.2 TPa [25]. The second type of inclusion, i.e. platelets, is prepared by exfoliating and separating the original material into platelets. One of the most common nano-plate inclusion is clay-based montmorillonite (MMT). The last type of particle is spherical particles. The most common material is silica (SiO_2) and precipitated calcium carbonate ($CaCO_3$). The size of the; unmodified $CaCO_3$ is about 80nm, and silica is between 10 to 500nm [25].

Agglomeration formation is the main issue in the distribution of the nanoparticles. Nano-sized particles tend to clump together, and the tendency increases with the decreasing particle size [63]. Formation of the agglomerations is hard to avoid. On the other hand, surface modification methods on the particles are employed, such as grafting the surface of the silica.

Carbon nanotubes (CNTs) are cylindrical nanoparticles with high aspect ratios. When the length of the CNT increases, particles entangle more easily and create flocs [37]. The agglomeration formation of CNTs can be seen in Figure 1.1 for the particles with high and low aspect ratios. It can be seen that the particles with high aspect ratios

tend to agglomerate more.

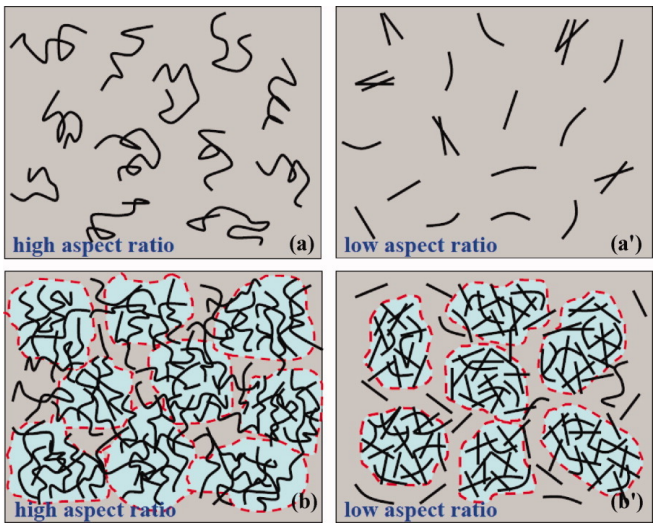


Figure 1.1: The illustration of the agglomeration formation relation with the aspect ratio of the carbon nanotubes [60]

1.2 Motivation and Aim of Thesis

Analytical calculations or experimental methods can calculate the overall mechanical properties of composite materials. On the other hand, these procedures are only available in limited scenarios, such as on large scales with aligned and homogeneously distributed inclusions with several assumptions, such as perfect materials and bonding. In the nano-scale, control of the homogeneity and alignment of the distribution of the inclusions is not feasible. Therefore, homogenization procedures are employed in this step to overcome this problem.

There are various methods of homogenization in literature, which can be classified and exemplified as; classical bounds as Voigt and Reuss; variational methods as Hashin-Shtrikman bounds; micromechanics-based approaches as the self-consistent scheme and Mori-Tanaka, etc. In this thesis, finite element method-based computational homogenization is employed to calculate the overall properties of the whole composite material.

The standard homogenization procedures generally assume the distribution of the particles is well-dispersed. On the other hand, numerous studies in the literature claim that particles are agglomerating, especially when nanocomposites are considered with high volume fraction. This effect should be considered since the aforementioned methods do not investigate this phenomenon.

In conclusion, this thesis aims to develop a realistic modeling approach for the nanocomposites and calculate the elastic constants more precisely, including the effects of the agglomerating particles. In addition to that, this study also aims to lower the computational cost. Since the procedure costs so much computational effort, some automatization algorithms are developed, and methods that ease the process are employed.

1.3 Scope and Roadmap of Thesis

As explained in the previous subsection, the following steps should be followed in the roadmap to achieve this objective. Firstly, the homogenization of randomly dispersed non-agglomerating particles in the matrix should be accomplished. The second step is to create a representative volume element with agglomerating particles and compare the results on overall mechanical properties. Therefore, the same initial distribution of particles should be considered in both cases.

To this end, several scripts are written to construct the representative volume elements with random non-agglomerating inclusions, detect and form agglomerates, and compute homogenized quantities. The first script, written in Python, creates the domain of the RVE for the random scattering of the inclusions. The domain is divided into smaller same-sized cubes, which are able to encapsulate only one particle. Therefore, the intersection between particles is prevented. In this domain, the locations of the inclusions are stored, and random coordinates are drawn from the prescribed domain. After the first script is run, random scattering of the particles and corresponding coordinates are achieved.

The second script is developed to detect the agglomeration phase using Matlab. If

nano-scale particles are close enough to each other to form an agglomeration phase, particles that form the agglomerated area are eliminated. Then, a spherical geometry representing the agglomeration phase is produced, which is large enough to enclose the vanished particles.

The third script is used for the generation of the RVE. ABAQUS runs a Python script and prepares the finite element model. Firstly, it generates the matrix and single inclusions, and agglomeration phases. After that, the prepared parts are translated to the corresponding coordinates taken from the second script. After materials are assigned to the corresponding parts, meshes are created, and proper boundary conditions relating to tensile and shear tests are applied. The displacement-driven tensile test simulations are conducted in the elastic range only. At the end of the third script, stress and strain values are ready to be processed.

Another script is developed to obtain the stress and strain values from each integration point of the model with Python. The matrix, single inclusions, and several agglomerations are scanned sequentially, and integration volumes, stress, and strains are gathered to calculate the homogenized material properties.

The last script is also developed in Matlab to calculate the elastic properties of the nanocomposite. This script needs homogenized stress and strain values from all six tests, i.e. three tensile and three shear tests. Homogenized elastic moduli, shear moduli, and Poisson's ratios are calculated using these inputs. These scripts and steps are explained further in the following chapters. Also, the theories behind these steps are explained in the methodology chapter. Scripts regarding periodic boundary condition implementation and homogenization can be seen in Appendix B.

These scripts are developed for both representative volume elements with agglomerating and non-agglomerating particles. The effect of agglomerating particles can be observed by comparing the results of the overall mechanical properties of these two RVEs. The results and discussions on results will be placed in the last chapter of the thesis before future work.

The following sets of studies are conducted to achieve the objective of the thesis. An RVE size study is conducted to find the minimum number of particles that is able to highlight the effect of agglomerations. A mesh convergence study is performed to determine the required element size. A comparison of the finite and embedded element methods is made. The effects of the different kinds of boundary conditions on results are examined. Finally, the results of the proposed approach are compared with the studies from the literature.

An overview, the motivation, the aim, the scope, and the roadmap of the thesis are presented in Chapter 1. In Chapter 2, general information about the methods and concepts that are used is given, and sample studies from the literature are presented. These methods and concepts are elaborated, and the theory behind these methods is explained in Chapter 3. The numerical solutions and several studies, such as mesh convergence, comparison of boundary conditions, and the comparison of the results with the experiments, are presented in Chapter 4. In the fifth chapter, the conclusion and future works are given.

CHAPTER 2

HOMOGENIZATION OF NANOCOMPOSITES

The homogenization of nanocomposite materials has been studied for some time in the literature. Numerous methods can be employed to homogenize a non-homogeneous media, and these methods are discussed in Chapter 3, with the method used in this thesis. A more comprehensive discussion on homogenization can be found in [47,56].

The workflow of the homogenization procedures can be eased by using some simplifications. In literature, the use of the embedded element method (EEM) and representative volume elements (RVE) is very common. An illustration can be seen in Figure 2.1. Sample studies of the aforementioned methods in homogenization are reviewed in the following sections.

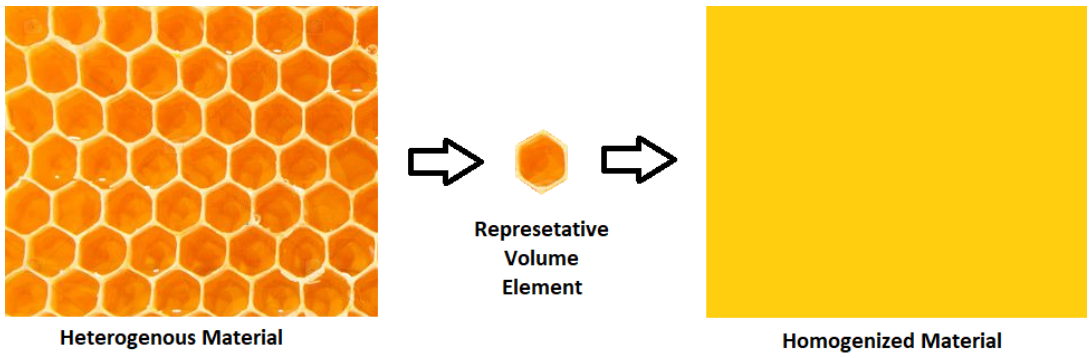


Figure 2.1: The illustration of the homogenization. The honeycomb structure is also used in the sandwich composites

2.1 Homogenization Methods

Two of the earliest and the most primitive methods are the very popular Voigt and Reuss bounds. Reuss and Voigt bounds give the lowest and highest possible elastic moduli for a heterogeneous media, respectively. The Voigt bound assumes the constant strain field [58], whereas the Reuss bound assumes the constant stress field [46] in heterogeneous media. An illustration of the Voigt and Reuss models can be seen in Figure 2.2.

Both Voigt and Reuss bounds use the elastic moduli and the volume fractions of the constituents. Neither of these methods takes into account the interaction between the phases as well as the topology of them. Any heterogeneous material's effective properties should be placed between these two bounds. Voigt and Reuss bounds read as:

$$E_{Voigt} = v_{fm}E_m + v_{fi}E_i \tag{2.1}$$

$$\frac{1}{E_{Reuss}} = \frac{v_{fm}}{E_m} + \frac{v_{fi}}{E_i}, \tag{2.2}$$

where v_{fm} and v_{fi} represent the volume fractions of matrix and inclusion, and E_m and E_i represent the elastic moduli of the matrix and the inclusion, respectively.

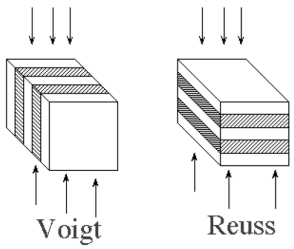


Figure 2.2: Illustrations of the models of Voigt and Reuss [30]

Hill average is calculated using Reuss and Voigt bounds. It basically takes the average of these two bounds. Therefore, topologies and the interaction between phases are not included. Hill average reads as:

$$E_{Hill\ average} = \frac{E_{Voigt} + E_{Reuss}}{2} \tag{2.3}$$

Another approach is the Hashin-Shtrikman which provides upper and lower bounds. Unlike Voigt and Reuss bounds, the Hashin-Shtrikman approach calculates the upper and lower bound based on the bulk modulus and shear modulus of the constituents by a variational approach [19]. The derivation of the effective property is based on strain energy minimization. The upper and lower bounds of this approach can be expressed as:

$$K_{HS+} = K_i + \frac{v_{fm}}{\frac{3v_{fi}}{3K_i+4G_i} + \frac{1}{K_m-K_i}} \tag{2.4}$$

$$K_{HS-} = K_m + \frac{v_{fi}}{\frac{3v_{fm}}{3K_m+4G_m} + \frac{1}{K_i-K_m}} \tag{2.5}$$

$$G_{HS+} = G_i + \frac{v_{fm}}{\frac{6v_{fi}(K_i+2G_i)}{5G_i(3K_i+4G_i)} + \frac{1}{G_m-G_i}} \tag{2.6}$$

$$G_{HS-} = G_m + \frac{v_{fi}}{\frac{6v_{fm}(K_m+2G_m)}{5G_m(3K_m+4G_m)} + \frac{1}{G_i-G_m}}, \tag{2.7}$$

where K_{HS+},K_{HS-},G_{HS+}, and G_{HS-} represent the upper and lower bounds of the bulk modulus and shear modulus, respectively. K_i,K_m,G_i, and G_m are the bulk modulus and the shear modulus of the inclusion and the matrix, respectively. Volume fractions of the inclusion and the matrix are represented with v_{fi} and v_{fm}, respectively. Equations 2.4-2.7 are valid for the materials with two constituents. The Hashin-Shtrikman principle can be applied to multi-phase models as well.

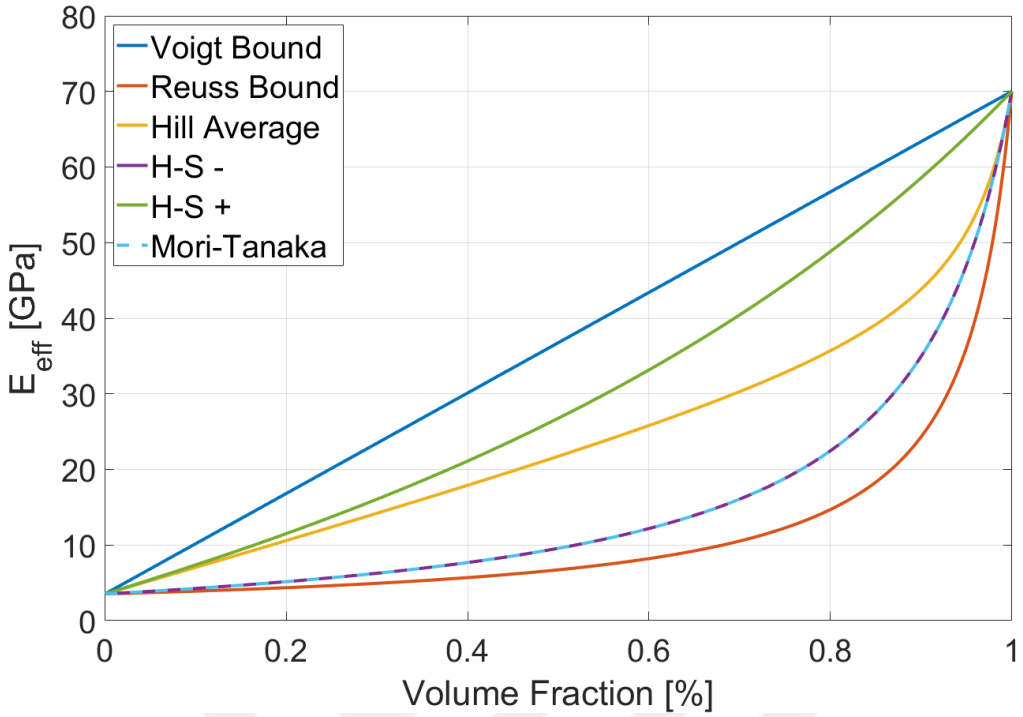


Figure 2.3: Comparison of the analytical homogenization techniques

The Voigt bound varies linearly with respect to volume fraction. The Voigt and Reuss create the upper and lower bound, while a narrower envelope is created with Hashin-Shtrikman bounds. The Hill average is inside of these bounds, as expected. The result of the Mori-Tanaka method gives the same results as the lower bound of the Hashin-Shtrikman method for an isotropic single spherical inclusion case [18]. Further information about the Mori-Tanaka method can be found in [36].

In order to demonstrate the predictions of these different approaches, a model composite system is considered. The matrix material is chosen as bis-phenol A, and the inclusion material is chosen as silica nanoparticle. The material properties are E_i=70GPa, E_m=3.53GPa, ν_i=0.17, and ν_m=0.35. The variation of the homogenized Young's modulus with volume fraction is depicted in Figure 2.3 for different approaches. The results are generated by developing a Matlab script.

2.2 Embedded Element Method

The embedded element method is employed to ease the meshing process of the RVE. In EEM, the elements of the embedded region are superimposed onto the elements of the host region. Therefore, a non-degenerated matrix geometry can be created. More comprehensive explanations and the theory can be found in Section 3.3.

The embedded element method used in the literature for homogenization to discretize inhomogeneous media. In the literature, the results of the homogenized mechanical properties obtained by the embedded element method and classical finite element method are compared.

Şık et al. [70] used the embedded element method in homogenization research that includes matrix non-linearity. In the study, homogenized mechanical property results of the classical finite element method, embedded element method, and a developed procedure with UMAT in ABAQUS are compared. Parametric studies are conducted, such as the effect of the element type, mesh density, boundary conditions, fiber volume fraction, and fiber stiffness. The results of the methods were compatible with each other.

Tabatabaei et al. [54, 55] conducted a comparison study between FEM and EEM. A single unidirectional fiber model, an irregularly distributed unidirectional fiber model, a single crimped yarn, and 5H satin-reinforced composite model are used in this comparison, as can be seen in Figure 2.4. The results of the elastic properties are compared and tabulated for 5H satin carbon/polyphenylene sulphide (PPS) composite. The difference in E_{xx}, E_{yy}, and E_{zz} (Young's modulus in different directions) are 0.25%, 0.39%, and 0.15%. Another set of results is tabulated for the irregularly distributed unidirectional fiber case. In this case, the difference in the results of E_{xx}, E_{yy}, and E_{zz} between the two methods are tabulated as 3.485%, 3.21%, and 1.30%. The differences show that the two methods can be replaced in necessary conditions.

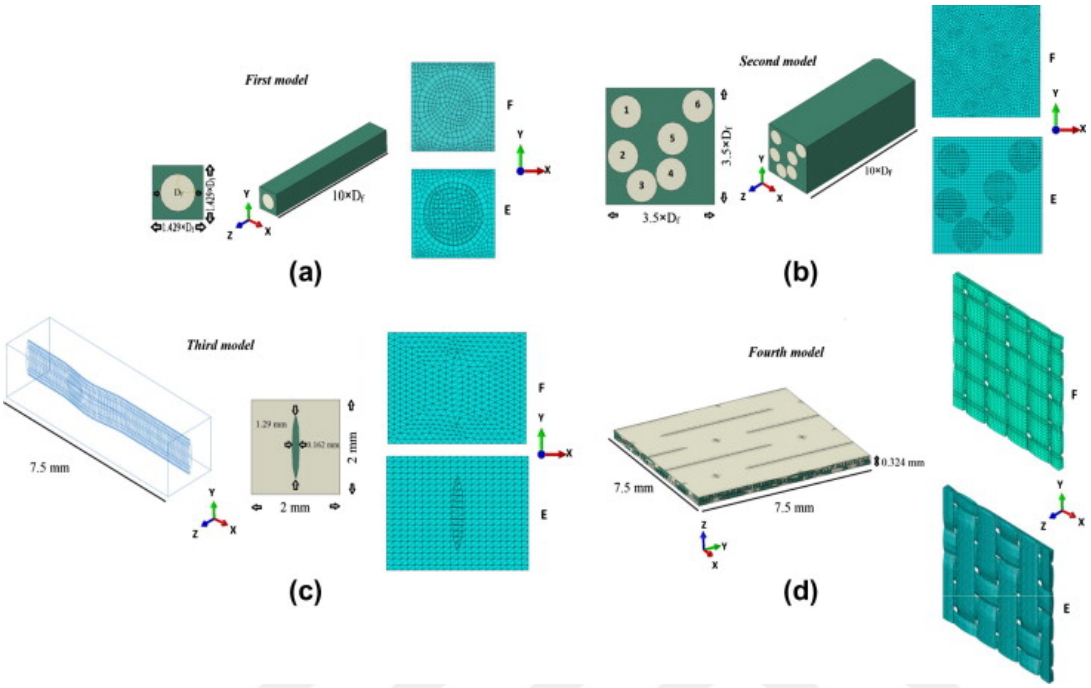


Figure 2.4: Illustrations of (a) single unidirectional fiber, (b) irregularly distributed unidirectional fiber, (c) a single crimped yarn, (d) 5H satin-reinforced composite models [53]

Another study comparing the homogenization results of the finite element and embedded element methods was conducted by Liu et al. [32]. Analytical methods such as Halpin-Tsai, Voigt, and Reuss bounds are also included. A discontinuous fiber is employed in the study, and homogenized mechanical properties are presented where the fibers are oriented randomly. Two RVEs are created with aligned and randomly dispersed short carbon fibers with an aspect ratio of 40 and 10, respectively. The volume fractions are taken as 30% and 10%, respectively. The RVEs are illustrated in Figure 2.5

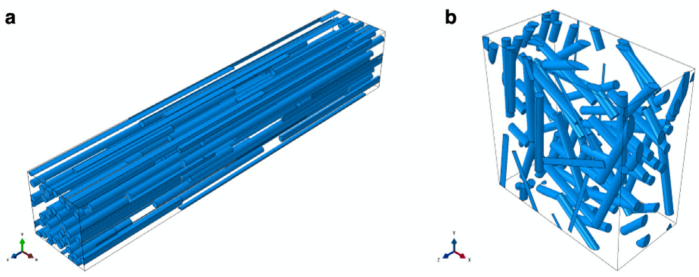


Figure 2.5: RVEs of; (a) Case a: aligned fibers with 30% volume fraction, and (b) Case b: randomly dispersed shot carbon fibers with 10% volume fraction [32]

The numerical results of the developed procedure are compared and tabulated with the results from the commercial homogenization software Digimat, which employs micromechanics (i.e. Eshelby's single inclusion and Mori-Tanaka) approaches [32]. The study results show good compatibility between the commercial software Digimat results and the embedded element method, as can be seen in Table 2.1.

Table 2.1: Comparison of the numerical and Digimat results for the cases [32]

	Case a		Case b	
Properties	Digimat	FEM	Digimat	FEM
$E_{11}(\mathrm{GPa})$	2.9302	3.4347	2.7382	2.8176
$E_{22}(\mathrm{GPa})$	2.9302	3.4951	2.5915	2.7453
$E_{33}(\mathrm{GPa})$	20.540	19.712	2.0903	2.1695
$G_{12}(\mathrm{GPa})$	0.98722	1.1591	0.99472	1.0467
$G_{23}(\mathrm{GPa})$	1.0744	1.3543	0.71036	0.74028
$G_{31}(\mathrm{GPa})$	1.0744	1.3049	0.70854	0.73819
μ_{12}	0.48406	0.42266	0.34558	0.33629
μ_{21}	0.48406	0.43010	0.32706	0.32766
μ_{13}	0.045703	0.055075	0.34547	0.34107

According to the above-mentioned studies that compare the EEM and FEM, the finite

element method can be replaced by the embedded element method if necessary.

2.3 Agglomeration

Particles in a matrix tend to clump together due to the attraction of the particles with each other via chemical bonds or van der Waals forces [66], as illustrated in Figure 2.6. This phenomenon depends on the particle size, distribution, and chemical properties of the particles.

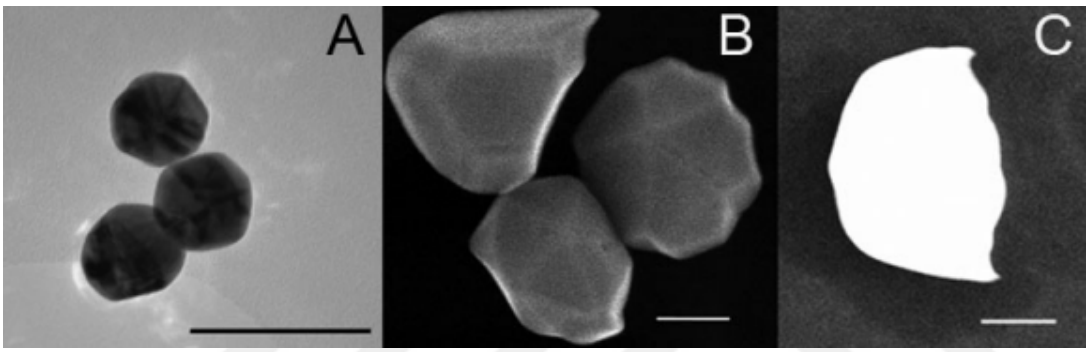


Figure 2.6: Transmission electron microscopy (TEM) image of (a) 50 nm gold particles, (b) 250 nm gold particles, (c) Example of a 250 nm gold particle. The bar length is 100 nm [14]

Dorigato et al. [9] studied filler aggregation as a reinforcement mechanism. Spherical-shaped fumed silica nanoparticles and glass microbeads are used as fillers, while linear low-density polyethylene (LLDPE) is used as the matrix. The particle sizes are 12nm and 7nm for the fumed silica particles Aerosil 200 and Aerosil 380, respectively, while it is 18μm for the glass microbeads. The mechanical properties of agglomerations are calculated using variational bounds derived by Hashin and Shtrikman. Up to 5$\%$ inclusion volume fractions are examined, and it is determined that the agglomeration phase reinforces the matrix. On the other hand, in the study of the Kontou and Niaounakis [28], the same materials used as the matrix and the inclusions as LLDPE and fumed silica nanoparticle (Aerosil R972 with the particle size of 16nm), and the degradation in the mechanical properties of the nanocomposite is

observed after 8% filler volume fraction. Consequently, it can be said that the filler volume fraction up to 5% is not sufficient to observe the degradation mechanism.

Zamanian et al. [64, 65] presented a study about the agglomeration effect on the elastic modulus. Silica nanoparticles are used as filler, and bisphenol as the matrix. Three different inclusion sizes, 12nm, 20nm, and 40nm, are used in the experiments, and the results are presented. In all sizes, a decrease in the elastic modulus after a particular filler loading is observed. In addition to that, the agglomeration effects are varied in different sizes. While particle size gets smaller, the agglomeration effect can be observed more clearly.

Kareem et al. [23] reviewed and evaluated the modeling of nanocomposite materials. In this study, analytical models are compared with an experiment. The experimental results are taken from the study of the Zamanian et al. [65]. Voigt and Reuss bounds, Halpin-Tsai model, Einstein, Guth, and Guth-Gold models are compared with the experimental result and presented. It is observed that the analytical methods can not catch the decrease at higher filler volume fractions, which is observed in the experimental results.

Demir et al. [8] studied the agglomeration effect in nanocomposites. In this study, cellulose nanocrystals (CNC) are used as filler and polyamide-6 as the matrix. The average CNC length and diameter are determined as 152nm and 6nm, respectively, after transmission electron microscopy (TEM) analysis. Random dispersion is satisfied by utilizing the Monte Carlo method. As in this thesis, the mechanical properties of the agglomeration phase are calculated using the inverse rule of mixture. The numerical results are compared with the experimental and analytical results. The experimental results show good compatibility with the numerical results, while a considerable difference is observed with the analytical results, as can be seen in Figure 2.7.

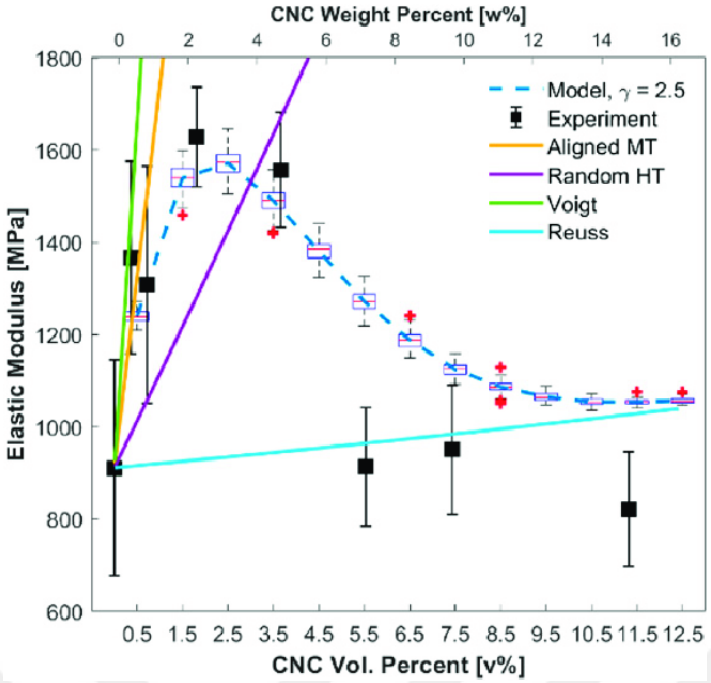


Figure 2.7: Comparison of the numerical, experimental, and analytical results of CNC/PA6 nanocomposite [8]

In Baek et al. [3], two cases, as RVE with and without agglomerations, were compared. In this study, the interphase effect is also included. Agglomerations are represented as clusters, and the RVE includes both clusters and free particles. Numerical results of the proposed method compared with the experimental results [5]. Isostatic polypropylene (PP) is used as the matrix, and non-grafted and grafted SiO_2 are used as particles with a radius of 9 Å. Experiments are compared with the present model with agglomerations and without agglomerations, as can be seen in Figure 2.8. The results show that the reinforcement degree is lower when the agglomeration effect is included.

Xie et al. [62] studied the rheological and mechanical properties of a nanocomposite. The matrix material is Poly(vinyl chloride), and the inclusion is calcium carbonate ($CaCO_3$) with an average size of 44nm. Predicted data and experimental results on Young's modulus are presented. A decrease after a five percent filler volume fraction is observed. Zare et al. [67] used this experimental data and proposed two approaches: The Kerner model and Paul's method. There is a difference in elastic modulus value

for both calculations. On the other hand, neither of these methods can simulate the decrease in the elastic modulus.

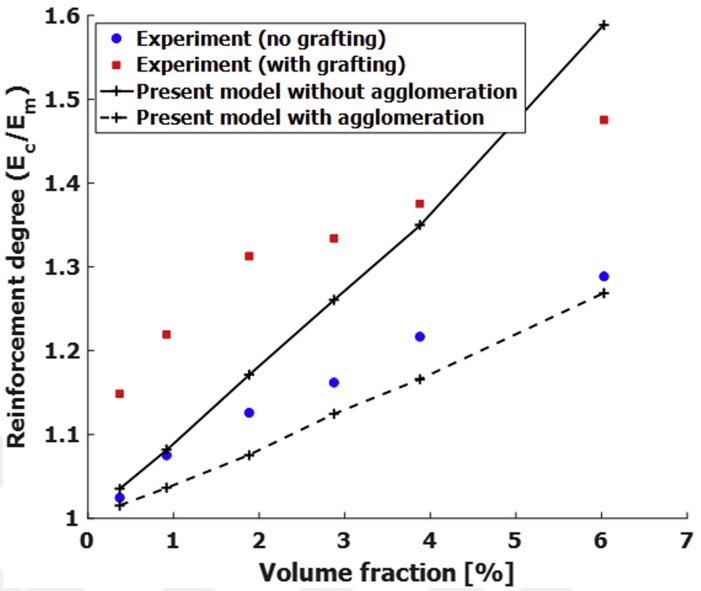


Figure 2.8: Comparison of the numerical and experimental results grafted and non-grafted particles for the cases with and without agglomerations [3]

It is clear from the results of the experiments that there is a decrease in the stiffness of the nanocomposite after some volume fractions. There are several approaches in the literature to explain the softening mechanism of agglomerations in nanocomposites. The softening mechanisms are explained further in the following paragraphs.

In nanocomposites, the interphase is the third phase formed between the filler and matrix due to the penetration and the entanglement of the polymer chains and chemical bonds. The interphase is a transition phase that shows the similar mechanical properties of the two other phases through thickness. The mechanical properties of this phase should be taken into account while calculating the overall mechanical properties of the nanocomposite because this phase affects the load transfer between the particle and the matrix [17]. Shin et al. [50] attribute the degradation in the mechanical property of the nanocomposite to the interphase overlapping. According to Shin et al. [50], agglomerations cause overlapping, which prevents the effective for-

mation of the interphase. Pontefisso et al. [43] studied the overlapping interphase phenomenon. An algorithm is generated for an easy-to-discretize RVE with overlapping interphases.

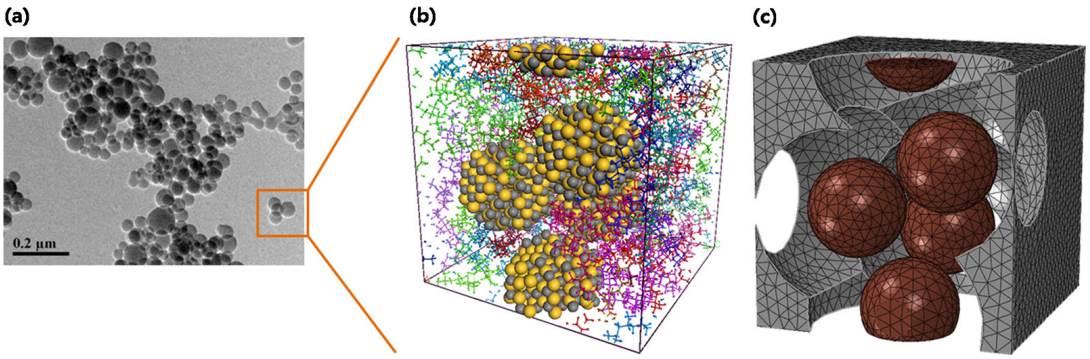


Figure 2.9: Illustrations of agglomerations: (a) TEM image [15], (b) molecular dynamics model, and (c) finite element model [50]

Baek et al. [3] conducted a nanocomposite homogenization in two steps considering the agglomerations effect based on interphase percolation. In this study, agglomerations are classified as clusters. First, clusters are homogenized, and in the second step, the RVE is homogenized. The clustering density and volume fraction and Young's modulus relations are presented in the study. The negative effect of the agglomerations on the mechanical properties is observed. The numerical results are compared with the experiment and tabulated.

According to [7,26], the enhancement of the mechanical properties may reduce by agglomerations due to the decrease in the interfacial area. Ashraf et al. [2] investigated and revealed the effects of the filler size and density on the surface area, specific surface area, and stiffening efficiency of the particles. Agglomerations are represented as large particles. In conclusion, they observed the negative effect of agglomerations on mechanical properties.

Fankhanel [11] approaches the degradation mechanism of agglomeration in an unusual way. The agglomeration phases are constructed by placing particles one by one

at a certain distance, as illustrated in Figure 2.10a. First, a particle is placed in the center of the simulation box. Then, a particular radius r is selected, so the second particle is placed on the radius randomly. A possible intersection is checked; if not, this agglomerate is shifted to the simulation box center. This procedure is repeated until the desired number of particles is reached. Once the agglomerate is formed, a resin-free area is searched. A resin-free area is a region between the particles that form the agglomerate, as illustrated in Figure 2.10b. This area is considered as empty. Therefore, this approach decreases the mechanical property of the nanocomposite.

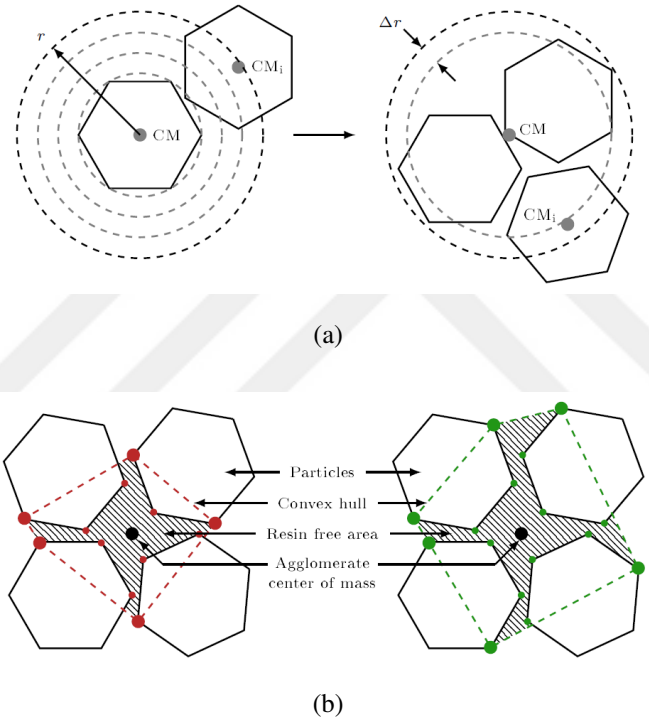


Figure 2.10: (a) Illustration of the placements of the particles and (b) the illustration of the resin-free area [11]

Overall, the degradation mechanism of the mechanical properties due to agglomerations is investigated and reported. The decrease in the specific surface or interfacial area due to the agglomeration degrades the homogenized elastic properties. The loss of the effective interphase volume is also reported as another mechanism causing

agglomeration-induced degradation in stiffness. In another study, the trapped volume inside the agglomeration is considered empty, leading to the degradation of elastic properties. The aforementioned studies conclude in the decrease of the surface due to agglomeration, in other words, the total contact area of the particles with the matrix.

In finite element models, the degradation of overall mechanical properties is satisfied by altering the elastic properties of the agglomeration phase. Different approaches can be employed, such as ignoring the resin-free area [11], decreasing the interphase volume [50], or altering the elastic modulus of the clusters using analytical methods such as the inverse rule of mixture [8].

CHAPTER 3

METHOD OF APPROACH

There are numerous methods to obtain the bulk material properties of a heterogeneous medium. Some of these methods do not consider the interaction between the phases, such as mixture rule models, while some others are limited to simple geometries, such as self-consistent methods. Finite element method-based computational homogenization is the method that is employed in this thesis. In this method, stress and strain values that are calculated at each integration point are used. All three phases in the model are discretized with linear hexagonal elements, which have eight integration points each. Since the loading scenario is inside the elastic range, stress and strain values are sufficient to calculate elasticity coefficients.

One uniaxial tension test in isotropic elasticity is sufficient to obtain Young's modulus and Poisson's ratio. For the uniaxial tensile test, displacement in one direction should be applied while displacements in other directions should be constrained. Since randomly distributed particles can lead to a slightly anisotropic response (see Appendix C), six tests are conducted to obtain elastic moduli, shear moduli, and Poisson's ratios in three directions.

3.1 Homogenization Method

Composite materials contain at least two materials with different mechanical properties, usually named matrix and filler. In the final product, the composite has its own mechanical properties, which are different from the included materials. In order to calculate the bulk material properties of the composite, inhomogeneous media should

be homogenized. There are numerous methods in the literature that can be used in homogenization. Computational, experimental, and analytical methods can be utilized to obtain bulk properties [16]. In this thesis, the computational homogenization method is used.

The elasticity constants of the nanocomposite can be calculated using uniaxial tension and shear tests. Then the material properties, i.e., the engineering constants, can be determined using elasticity constants. The computational homogenization method uses stress, strain, and volume values from each integration point in each element in the model.

The elasticity tensor should be examined before calculating elastic constants. This tensor expresses the relation between strain and stress. It is a fourth-order tensor with eighty-one components. On the other hand, the minor symmetry condition decreases from 81 components to 36 if the tensor satisfies the following relation:

$$C_{ijkl} = C_{jikl} \qquad \text{and} \qquad C_{ijkl} = C_{ijlk} \tag{3.1}$$

As well as minor symmetry, the elasticity tensor has major symmetry. Major symmetry conditions can be seen in the following relation.

$$C_{ijkl} = C_{klij} \tag{3.2}$$

The number of coefficients of the fourth-order tensor with minor and major symmetries decreases to 21 from 81. A simplified matrix representation of the elasticity tensor is as follows:

$$\begin{bmatrix} \sigma_{11} \\ \sigma_{22} \\ \sigma_{33} \\ \sigma_{23} \\ \sigma_{13} \\ \sigma_{12} \end{bmatrix} = \begin{bmatrix} C_{1111} & C_{1122} & C_{1133} & C_{1123} & C_{1113} & C_{1112} \\ & C_{2222} & C_{2233} & C_{2223} & C_{2213} & C_{2212} \\ & & C_{3333} & C_{3323} & C_{3313} & C_{3312} \\ & & & C_{2323} & C_{2313} & C_{2312} \\ & & & & C_{1313} & C_{1312} \\ & \text{sym} & & & & C_{1212} \end{bmatrix} \begin{bmatrix} \varepsilon_{11} \\ \varepsilon_{22} \\ \varepsilon_{33} \\ 2\varepsilon_{23} \\ 2\varepsilon_{13} \\ 2\varepsilon_{12} \end{bmatrix} \tag{3.3}$$

The elasticity tensor can be rewritten in Voigt notation, also. In this notation, engineering shear strains can be rewritten as $2\varepsilon_{23} = \varepsilon_4$, $2\varepsilon_{13} = \varepsilon_5$, and $2\varepsilon_{12} = \varepsilon_6$.

$$\begin{bmatrix} \sigma_1 \\ \sigma_2 \\ \sigma_3 \\ \sigma_4 \\ \sigma_5 \\ \sigma_6 \end{bmatrix} = \begin{bmatrix} C_{11} & C_{12} & C_{13} & C_{14} & C_{15} & C_{16} \\ & C_{22} & C_{23} & C_{24} & C_{25} & C_{26} \\ & & C_{33} & C_{34} & C_{35} & C_{36} \\ & & & C_{44} & C_{45} & C_{46} \\ & & & & C_{55} & C_{56} \\ & \text{sym} & & & & C_{66} \end{bmatrix} \begin{bmatrix} \varepsilon_1 \\ \varepsilon_2 \\ \varepsilon_3 \\ \varepsilon_4 \\ \varepsilon_5 \\ \varepsilon_6 \end{bmatrix} \tag{3.4}$$

The orthotropic materials are materials with three mutually orthogonal planes of symmetry. For an orthotropic material, the stress-strain relation, when written in a coordinate system aligned with the axes of orthotropy, can be further simplified to:

$$\begin{bmatrix} \sigma_1 \\ \sigma_2 \\ \sigma_3 \\ \sigma_4 \\ \sigma_5 \\ \sigma_6 \end{bmatrix} = \begin{bmatrix} C_{11} & C_{12} & C_{13} & 0 & 0 & 0 \\ & C_{22} & C_{23} & 0 & 0 & 0 \\ & & C_{33} & 0 & 0 & 0 \\ & & & C_{44} & 0 & 0 \\ & & & & C_{55} & 0 \\ & \text{sym} & & & & C_{66} \end{bmatrix} \begin{bmatrix} \varepsilon_1 \\ \varepsilon_2 \\ \varepsilon_3 \\ \varepsilon_4 \\ \varepsilon_5 \\ \varepsilon_6 \end{bmatrix} \tag{3.5}$$

Six linear equations can be written from the stress-strain relation for an orthotropic material:

$$
\begin{aligned}
\sigma_1 &= C_{11}\varepsilon_1 + C_{12}\varepsilon_2 + C_{13}\varepsilon_3 \\
\sigma_2 &= C_{12}\varepsilon_1 + C_{22}\varepsilon_2 + C_{23}\varepsilon_3 \\
\sigma_3 &= C_{13}\varepsilon_1 + C_{23}\varepsilon_2 + C_{33}\varepsilon_3 \\
\sigma_4 &= C_{44}\varepsilon_4 \\
\sigma_5 &= C_{55}\varepsilon_5 \\
\sigma_6 &= C_{66}\varepsilon_6
\end{aligned}
\tag{3.6}
$$

Six displacement-driven tests are necessary to obtain the nine coefficients in the elasticity tensor. Six load cases are applied as follows, while the first three loadings in Equation 3.7 correspond to the uniaxial tests, the last three loadings correspond to the shear tests.

$$
\begin{aligned}
&\begin{bmatrix} \delta & 0 & 0 \\ 0 & 0 & 0 \\ 0 & 0 & 0 \end{bmatrix} = \boldsymbol{\varepsilon}_1 \quad \begin{bmatrix} 0 & 0 & 0 \\ 0 & \delta & 0 \\ 0 & 0 & 0 \end{bmatrix} = \boldsymbol{\varepsilon}_2 \quad \begin{bmatrix} 0 & 0 & 0 \\ 0 & 0 & 0 \\ 0 & 0 & \delta \end{bmatrix} = \boldsymbol{\varepsilon}_3 \\
&\begin{bmatrix} 0 & \delta & 0 \\ \delta & 0 & 0 \\ 0 & 0 & 0 \end{bmatrix} = \boldsymbol{\varepsilon}_4 \quad \begin{bmatrix} 0 & 0 & 0 \\ 0 & 0 & \delta \\ 0 & \delta & 0 \end{bmatrix} = \boldsymbol{\varepsilon}_5 \quad \begin{bmatrix} 0 & 0 & \delta \\ 0 & 0 & 0 \\ \delta & 0 & 0 \end{bmatrix} = \boldsymbol{\varepsilon}_6
\end{aligned}
\tag{3.7}
$$

In 3.7, δ stands for a constant load. C_{11}, C_{12}, and C_{13} can be obtained as a result of one uniaxial tension test while restricting displacements in other directions, as it is stated in Equation 3.7:

$$
\begin{aligned}
\sigma_1 &= C_{11}\varepsilon_1 + C_{12}\cancelto{0}{\varepsilon_2} + C_{13}\cancelto{0}{\varepsilon_3} \\
\sigma_2 &= C_{12}\varepsilon_1 + C_{22}\cancelto{0}{\varepsilon_2} + C_{23}\cancelto{0}{\varepsilon_3} \\
\sigma_3 &= C_{13}\varepsilon_1 + C_{32}\cancelto{0}{\varepsilon_2} + C_{33}\cancelto{0}{\varepsilon_3}
\end{aligned}
\tag{3.8}
$$

Similarly, applying normal strain in direction 2 while restricting deformations in directions 1 and 3 gives the coefficients of C_{12}, C_{22}, and C_{23}.

$$\begin{aligned}
\sigma_1 &= C_{11}\cancelto{0}{\varepsilon_1} + C_{12}\varepsilon_2 + C_{13}\cancelto{0}{\varepsilon_3} \\
\sigma_2 &= C_{12}\cancelto{0}{\varepsilon_1} + C_{22}\varepsilon_2 + C_{23}\cancelto{0}{\varepsilon_3} \\
\sigma_3 &= C_{13}\cancelto{0}{\varepsilon_1} + C_{32}\varepsilon_2 + C_{33}\cancelto{0}{\varepsilon_3}
\end{aligned} \tag{3.9}$$

Likewise, the application of the same steps for direction 3 results in obtaining C_{13}, C_{23}, and C_{33}.

$$\begin{aligned}
\sigma_1 &= C_{11}\cancelto{0}{\varepsilon_1} + C_{12}\cancelto{0}{\varepsilon_2} + C_{13}\varepsilon_3 \\
\sigma_2 &= C_{12}\cancelto{0}{\varepsilon_1} + C_{22}\cancelto{0}{\varepsilon_2} + C_{23}\varepsilon_3 \\
\sigma_3 &= C_{13}\cancelto{0}{\varepsilon_1} + C_{32}\cancelto{0}{\varepsilon_2} + C_{33}\varepsilon_3
\end{aligned} \tag{3.10}$$

To obtain the elastic coefficients of C_{44}, C_{55}, and C_{66}, simple shear deformations are applied, and the following relations are used:

$$\begin{aligned}
\sigma_4 &= C_{44}\varepsilon_4 \\
\sigma_5 &= C_{55}\varepsilon_5 \\
\sigma_6 &= C_{66}\varepsilon_6
\end{aligned} \tag{3.11}$$

The elasticity matrix can be obtained at the end of the previous calculations. The compliance matrix $(\mathbf{S})$ can be obtained by taking the inverse of the elasticity matrix.

$$\mathbf{S} = \mathbf{C}^{-1} \tag{3.12}$$

The compliance matrix for an orthotropic material reads:

$$\begin{bmatrix} \varepsilon_{xx} \\ \varepsilon_{yy} \\ \varepsilon_{zz} \\ \varepsilon_{xz} \\ \varepsilon_{yz} \\ \varepsilon_{xy} \end{bmatrix} = \begin{bmatrix} \frac{1}{E_x} & \frac{-\nu_{yx}}{E_y} & \frac{-\nu_{zx}}{E_z} & 0 & 0 & 0 \\ \frac{-\nu_{xy}}{E_x} & \frac{1}{E_y} & \frac{-\nu_{zy}}{E_z} & 0 & 0 & 0 \\ \frac{-\nu_{xz}}{E_x} & \frac{-\nu_{yz}}{E_y} & \frac{1}{E_z} & 0 & 0 & 0 \\ 0 & 0 & 0 & \frac{1}{2G_{xz}} & 0 & 0 \\ 0 & 0 & 0 & 0 & \frac{1}{2G_{yz}} & 0 \\ 0 & 0 & 0 & 0 & 0 & \frac{1}{2G_{xy}} \end{bmatrix} \begin{bmatrix} \sigma_{xx} \\ \sigma_{yy} \\ \sigma_{zz} \\ \sigma_{xz} \\ \sigma_{yz} \\ \sigma_{xy} \end{bmatrix} \tag{3.13}$$

Material properties (E_x, E_y, E_z, G_{xz}, G_{yz}, G_{xy}, ν_{xy}, ν_{xz}, ν_{yz}) can be found using Equation 3.13. The above matrix is turned into a system of linear equations, and a Matlab script is developed to achieve the aforementioned properties.

The literature generally reports experimental data as a single Young's modulus value. To this end, an average Young's modulus term $\bar{E}$ in terms of engineering constants E_x, E_y, and E_z is introduced as follows.

$$\bar{E} = \frac{E_x + E_y + E_z}{3} \tag{3.14}$$

Later, $\bar{E}$ will be used to compare with the experimental results.

3.1.1 Finite Element Model of the RVE

The finite element model is generated using a Python-based script. This script includes every step of the model construction, such as a sketch of the inclusion, matrix, and various-sized agglomerations, the partition of the geometry in order to generate an adequate mesh, material properties of each phase and their assignments, creation of the assembly, arrangement of the step size, application of the interactions and contact algorithms, request of the outputs, meshing and the execution. Such a script should be developed since the locations of the nanoparticles are random and change in each simulation scenario. Numerous studies have been conducted to create the finite element model in order to achieve the most realistic simulation, such as "*convergence with the number of particles*" and "*mesh convergence*" studies. These studies will be explained further in detail in Chapter 4.

3.1.2 Random Sequential Adsorption Algorithm

The dispersion of the particles inside the RVE is random in many applications. To simulate randomness, a random dispersion algorithm must be employed. Random sequential adsorption, modified random sequential adsorption, collective rearrangement, Monte Carlo, and random walk approaches can be employed to obtain random dispersion. There are advantages and disadvantages of each algorithm [1].

RSA algorithm places the inclusions sequentially in a prescribed volume while preventing the intersections between particles. After the placement of the first particle, the coordinate of that particle becomes fixed and can not be used for the next particles. The second particle is placed in a position that, in the direction of a random vector, originated from the first particle. The distance between the particles should be a minimum of at least one particle size in order to prevent intersection. This procedure continues until the desired volume fraction is reached, as in the study of Zhou et al. [69]. Further and more detailed information can be found in [59], [68].

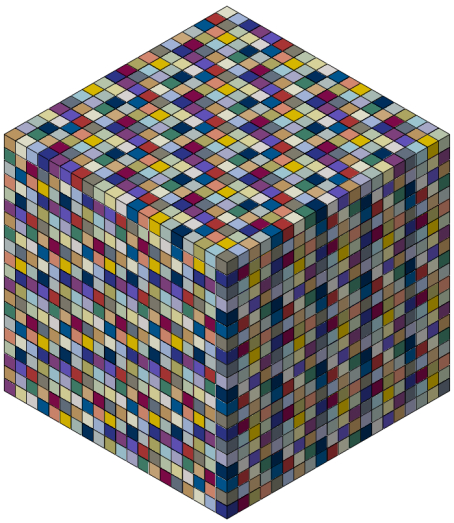


Figure 3.1: An illustration of the domain divided into small pieces in the size of the particles

This method can also be applied by dividing the domain into smaller pieces which only one spherical inclusion can barely fit into it, as illustrated in Figure 3.1. Therefore, the possible coordinates of the particles are fixed. The division prevents the intersection of the particles. There is only one scenario left for the intersection, which is the random choice of the same coordinate for more than one particle. This algorithm also prevents this phenomenon by choosing available coordinates sequentially. In this way, once one coordinate is chosen for one particle, that coordinate would no longer be available. This method enforces to place same sized particles since the sizes of the divided pieces are the same. On the other hand, this limitation does not cause any problems since the particle sizes are the same in the thesis.

3.1.3 Representative Volume Element

Construction of the finite element model of the whole nanocomposite structure by discretizing all nano-inclusions is not suitable due to the concern of computational cost. Instead, a piece of the whole part can be used to represent the whole part, as illustrated in Figure 3.2. The chosen small piece has to show the same mechanical properties as the whole material. In addition to that, the stored strain energy densities should be the same in RVE and the whole material [4].

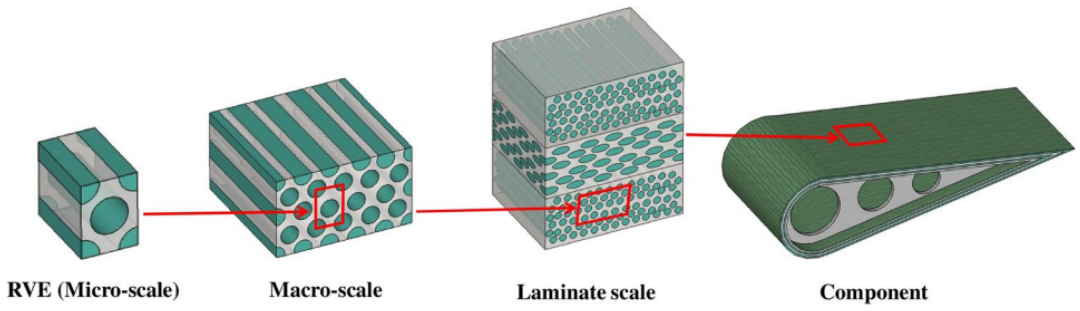


Figure 3.2: An RVE Sample from a Composite Component [39]

Since a heterogeneous medium is studied in this thesis, the RVE geometry and size can not be chosen randomly. The constructed RVE should contain a similar level of

heterogeneity as the whole composite. Any RVE that contains one inclusion could be selected in the matrix if the inclusions were distributed uniformly and aligned.

The choice of the RVE also affects the cost of the calculation. This parameter is important since the aim of the RVE is to decrease the computational cost by saving time and memory.

In conclusion, due to the reasons that are explained in the above paragraphs, an RVE size study is conducted to decide the optimum RVE size. The method and the results of this study are explained in Chapter 4.

3.1.4 Boundary Condition

The selection of the boundary condition type is important. On the other hand, independent of choice, the boundary condition should satisfy some physical/mathematical conditions.

The condition for the equivalence of energetically and mechanically defined effective properties of inhomogeneous media is known as the Hill principle or Hill-Mandel macro homogeneity condition [20]. Detailed information about the Hill condition can be found in [22], [38].

Several common types of boundary conditions practiced in engineering can be applied to RVE, such as linear displacement (Dirichlet type), constant traction (Neumann type), and periodic boundary conditions that satisfy the Hill condition [41], [40], [21]. For a linear elastic material, Hill's energy principle can be expressed as:

$$\overline{\boldsymbol{\sigma} : \boldsymbol{\varepsilon}} = \bar{\boldsymbol{\sigma}} : \bar{\boldsymbol{\varepsilon}} \tag{3.15}$$

The above bar in Equation 3.15 represents the spatial average. Hill's principle states that the double contraction of the stress and strain tensor's average is the same as the double contraction of the average stress and strain tensors.

The volume average of a variable $f(x)$ can be calculated for an RVE with the volume of V as follows:

$$\bar{f} = \frac{1}{V}\int_V f(x)dV \tag{3.16}$$

Therefore, the averages of stress and strain can be calculated as follows:

$$\bar{\boldsymbol{\varepsilon}} = \frac{1}{V}\int_V \boldsymbol{\varepsilon}(\boldsymbol{x})dV \tag{3.17}$$

$$\bar{\boldsymbol{\sigma}} = \frac{1}{V}\int_V \boldsymbol{\sigma}(\boldsymbol{x})dV \tag{3.18}$$

Using divergence theorem, Equations 3.18 and 3.17 leads as follows:

$$\bar{\boldsymbol{\varepsilon}} = \frac{1}{V}\int_\Gamma \boldsymbol{u}(\boldsymbol{x}) \otimes \boldsymbol{n}(\boldsymbol{x})d\Gamma \tag{3.19}$$

$$\bar{\boldsymbol{\sigma}} = \frac{1}{V}\int_\Gamma \boldsymbol{t}(\boldsymbol{x}) \otimes \boldsymbol{x}d\Gamma, \tag{3.20}$$

where Γ represents the surface of the RVE, $\boldsymbol{x}$ is the position of the nodes on the surface, $\boldsymbol{n}$ is the surface normal vector, $\boldsymbol{t}(\boldsymbol{x})$ is surface traction vector, and $\boldsymbol{u}(\boldsymbol{x})$ is the displacement vector. Body forces are neglected, and the equations apply for linear elastic behavior only.

$$\overline{\boldsymbol{\sigma}\boldsymbol{\varepsilon}} = \frac{1}{V}\int_V \boldsymbol{\sigma}(\boldsymbol{x})\boldsymbol{\varepsilon}(\boldsymbol{x})dV \tag{3.21}$$

Equations 3.17-3.21 results in Equation 3.22:

$$\int_\Gamma \left(t_i - \bar{\sigma}_{ij}n_j\right)\left(u_i - \bar{\varepsilon}_{ik}x_k\right)d\Gamma = 0 \tag{3.22}$$

Equation 3.22 can be satisfied by canceling the first or second term to zero. Therefore, two options are acquired, leading to the displacement and the traction boundary con-

ditions. A brief introduction to different boundary condition types is given next. Further information and details about boundary conditions can be accessed from [12,48].

Displacement Boundary Condition

Displacement boundary condition (DBC) is defined as uniform displacement values on the surface of the RVE. The displacement boundary condition stands as follows:

$$u_i = \bar{\varepsilon}_{ij} x_j \qquad \forall \boldsymbol{x} \in \Gamma, \tag{3.23}$$

where $\bar{\varepsilon}_{ij}$ represents the average strain, u_i is the displacement vector, and x_j is the coordinate of the nodes on the surface of the RVE. This equity satisfies the Hill condition.

Traction Boundary Condition

Traction boundary condition (TBC) is defined as uniform traction values on the surface of the RVE. The traction boundary condition stands as follows:

$$t_i = \bar{\sigma}_{ij} n_j \qquad \forall \boldsymbol{x} \in \Gamma, \tag{3.24}$$

where $\bar{\sigma}_{ij}$ represents the average stress, t_i is the traction vector, and n_j is the outward unit normal at the integration point on the surface elements.

Periodic Boundary Condition

A representative volume element illustrates the macroscopic behavior of the composite material. In other words, periodically placed RVEs in all directions construct the whole material [29]. This phenomenon should be maintained even in the deformed shape of the RVE. To this end, periodic boundary conditions (PBC) satisfy this condition. The application of periodic boundary conditions can be found in [52]. PBC ensures that the deformed RVEs do not penetrate with each other, and every RVE just

fits into the neighbor ones. In other words, there exists no gap between deformed RVEs, which is a must. In this finite element model, nodes are symmetrical on the opposite faces of the RVE. This gives an advantage in the implementation of the PBC into the finite element model.

Pahr and Böhm [41] employ the terms south (S), north (N), east (E), west (W), top (T), and bottom (B) to designate the surfaces of the RVE. Also, the corner nodes and edges are named accordingly, as illustrated in Figure 3.3.

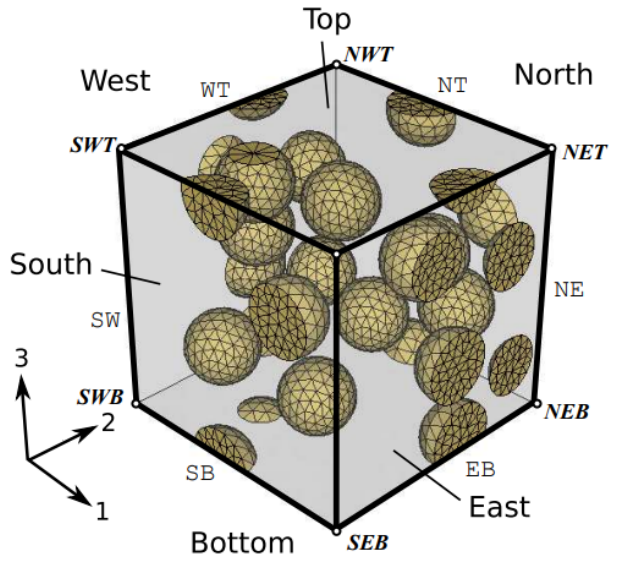


Figure 3.3: Illustration of the RVE with randomly distributed spherical inclusions with a 15% volume fraction. The surfaces, corner nodes, and edges are named using directions: east, west, north, south, top, and bottom [41]

As explained previously, the deformed shape of the opposite surfaces (north-south, west-east, and top-bottom) of the RVE should be precisely the same. This condition can be satisfied by constraining the nodes on the opposite surfaces in three degrees of freedom (DOF). The displacement between a pair of nodes is expressed as follows:

$$\Delta \boldsymbol{u}_k = \boldsymbol{u}_{k^+} - \boldsymbol{u}_{k^-} = \boldsymbol{u}(\boldsymbol{s_k} + \boldsymbol{c_k}) - \boldsymbol{u}(\boldsymbol{s_k}) = \bar{\boldsymbol{\varepsilon}} \boldsymbol{c}_k, \tag{3.25}$$

where, $\boldsymbol{s}_k$ and $\boldsymbol{s}_k + \boldsymbol{c}_k$ represents the positions of the pair of nodes, while $\boldsymbol{c_k}$ is the shift vector. A shift vector is introduced since the pair of nodes are shifted relative to each other after the applied boundary condition, as illustrated in Figure 3.4. By using designations that are presented in Figure 3.3, Equation 3.25 leads to:

$$\boldsymbol{u}_N(\tilde{s}_1) = \boldsymbol{u}_S(\tilde{s}_1) + \boldsymbol{u}_{NW} \qquad \text{and} \qquad \boldsymbol{u}_E(\tilde{s}_2) = \boldsymbol{u}_W(\tilde{s}_2) + \boldsymbol{u}_{SE}, \tag{3.26}$$

where $\tilde{s_k}$ represents the local coordinates of the paired nodes on the surface. Equation 3.26 leads to:

$$\boldsymbol{u}_{NE} = \boldsymbol{u}_{SE} + \boldsymbol{u}_{NW} \tag{3.27}$$

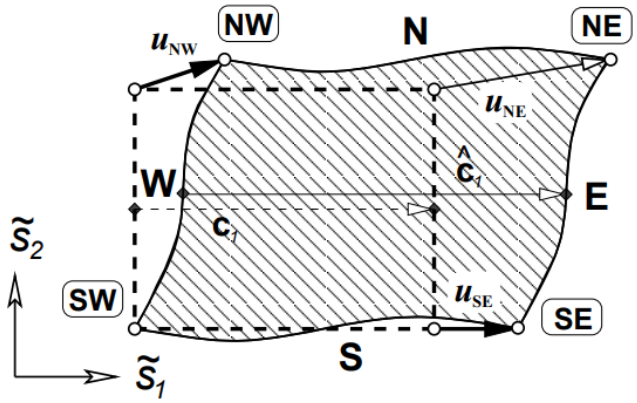


Figure 3.4: Illustration of the periodic boundary condition applied deformed rectangular two-dimensional RVE [6]

A study is conducted to determine the use of uniform displacement and periodic boundary conditions for a smaller RVE containing only one spherical nano-inclusion. The elastic properties are calculated, and the results are compared. At the end of the study, for the RVE with multi-inclusions, linear displacement type boundary condition is applied to the original RVE, as illustrated in Figure 3.5, since the number of constraints reasoning by periodic boundary conditions is too much, and modeling is infeasible. Further details and the comparison study are explained in Chapter 4.

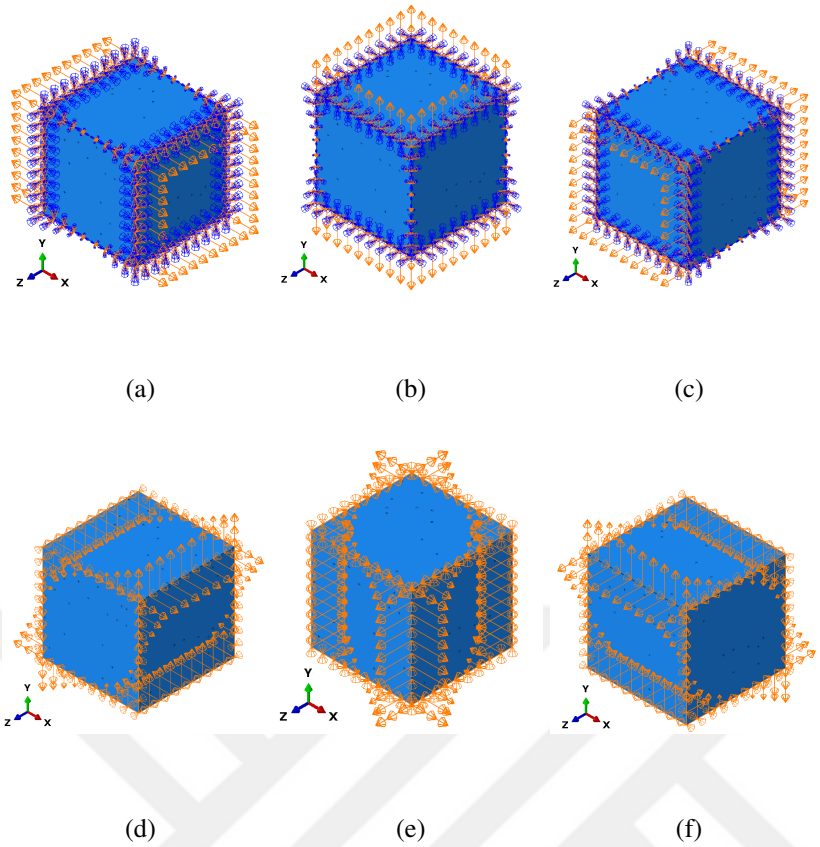


Figure 3.5: Applied displacement boundary conditions. Uniaxial tensile tests in (a) x-direction, (b) y-direction, (c) z-direction, and shear tests in (d) xy-plane, (e) xz-plane, and (f) yz-plane

3.2 Formation of the Agglomeration

The agglomerations are formed inside the RVE by clumped together particles. The coordinates of the randomly dispersed particles are stored to detect the agglomerations. The agglomerations are formed by choosing and vanishing the close particles and placing a larger particle that is large enough to enclose the pre-chosen particles. The *smallest* sphere that encapsulates the vanished particles is placed as an agglomerate.

Close particles are detected by using a new term called *critical distance*. Critical

distance determines if the particles are close enough to form an agglomeration phase. The critical distance is the distance between two particles' centers, as illustrated in Figure 3.6. Therefore, it can be chosen such that $2r$ as sticking particles, $4r$ as two particles that can fit another particle between them.

The critical distance value can be affected by several parameters. As stated in Chapter 2, smaller particles tend to agglomerate due to their high specific surfaces. Therefore, particle size can be a parameter to determine the value of the critical distance. Besides particle size, surface treatment procedures can be employed to prevent the formation of agglomerations. These methods also affect the determination of the critical distance. Since agglomeration formation would be less in the case of functionalized particles, lower values of critical distance can be chosen in the modeling of the RVE.

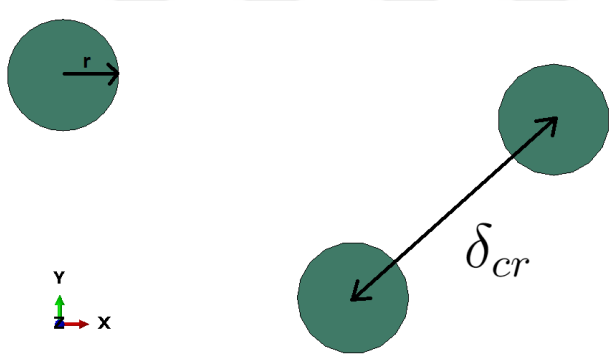


Figure 3.6: Illustration of the critical distance between randomly dispersed particles. The minimum value of the critical distance is $2r$

Different numbers of particles form different-sized agglomerations. If another particle is inside the range of the critical distance, the agglomeration enlarges to encapsulate the third particle, and the center of the agglomeration changes accordingly. If three particles are inside the range of the critical distance, more than one intersecting agglomeration is formed, as illustrated in Figure 3.7. To avoid such a situation, a control script is developed to prevent the formation of the agglomerations of two, instead, to form the agglomeration of three particles, as in Figure 3.8. The control script prevents the intersection of the agglomerations. The script checks the distance between agglomerations. If the distance between agglomerations is smaller than the diameters

of the agglomerations (i.e. intersection is detected), the agglomerations vanish, and a larger agglomeration (i.e. including three particles) is formed.

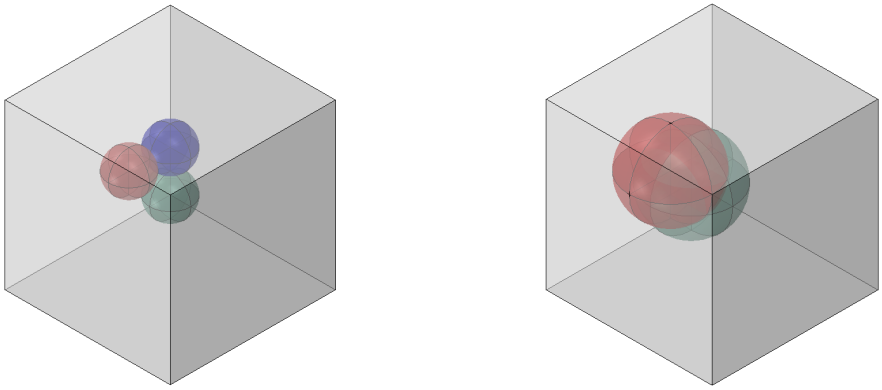


Figure 3.7: Illustration of agglomeration formation without control script

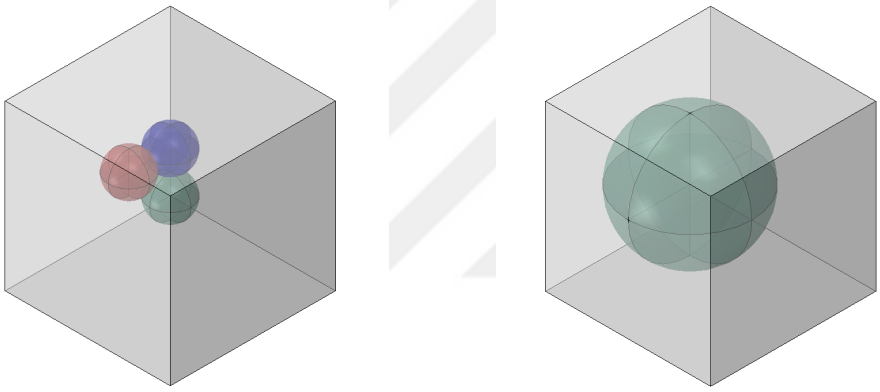


Figure 3.8: Illustration of agglomeration formation with control script

The mechanical properties of the agglomerations are calculated for each size of agglomeration. The inverse rule of mixtures is employed to calculate the elastic properties, as proposed in Demir et al. [8].

$$\frac{1}{E_{agg}} = \frac{v_{fmat}}{E_{mat}} + \frac{v_{finc}}{E_{inc}} \tag{3.28}$$

Young's modulus of the agglomerate (E_{agg}) is calculated using the volume fraction of the matrix v_{fmat} and the volume fraction of the inclusion v_{finc}. E_{mat} and E_{inc} denote Young's modulus of the matrix and the inclusion, respectively. The same procedure

can also be applied to Poisson's ratio [42]. The volume fractions of the inclusions and matrix inside the agglomerates are calculated, and the mechanical properties of the agglomerations are computed for the agglomerations in each size.

3.3 Embedded Element Method

The embedded element method is used to ease the computational cost. In the classical finite element method, the geometry of the matrix is porous-like due to inclusions. The matrix and the nanoparticles should be discretized in such a way that the nodes at the boundary between the particles and matrix geometry are matched. Creating this model may consume too much pre-processing effort, and a structured mesh on the matrix is tough to get. In the embedded element method, there is no need to create such a matrix geometry. Matrix and inclusion geometries are discretized separately, but since geometry partition is unnecessary for this method, meshing is much easier.

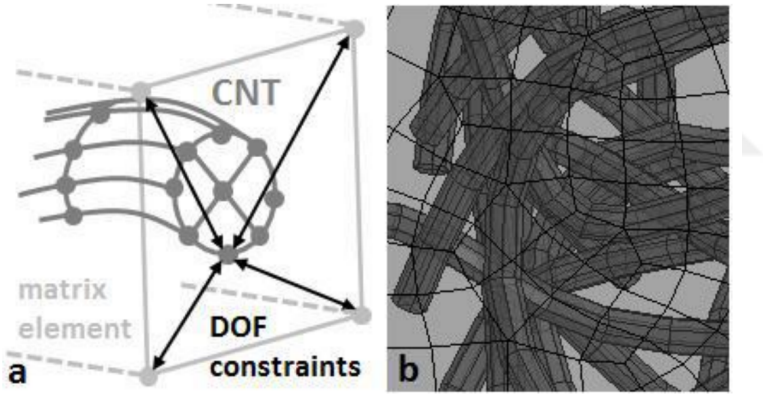


Figure 3.9: (a) Schematic of the constraint between embedded and host nodes, (b) illustration of the multi-carbon nanotube model [34]

This method divides the model into two regions: the host region and the embedded region [51]. The host region is defined by matrix geometry. On the other hand, the embedded regions are defined for each inclusion and agglomeration. Then, interactions are defined between these two regions. Since the number of embedded regions may be very high in some simulations, this phenomenon results in too many constraints in an RVE with randomly distributed particles. Therefore, a script should be

developed to automate this process.

The contact or interaction algorithm in this method is different than usual. In regular contact algorithms, a pair of surfaces is selected, and contact is assigned between these master and slave surfaces. However, there is no surface that acts as a master surface. In this method, all of the nodes of the embedded region and host region are connected to each other, as illustrated in Figure 3.9. The translational DOFs of the nodes belonging to the embedded region are eliminated and constrained to the DOF of the nodes belonging to the host region [13]. These constraints are provided by interpolating the DOFs of the host elements considering the distance (geometric relation) to the nodes of the embedded elements. The weight functions are used in ABAQUS as follows [44]:

$$U_{i(E)} = \sum_{j=1}^{N} W_j U_{j(H)}, \tag{3.29}$$

where $U_{i(E)}$ and $U_{j(H)}$ stand for the DOF of the embedded nodes and the host nodes, respectively. W_j stands for the weight function, which is related to the distance between the aforementioned nodes. While the distance between the nodes increases, the value of the weight function decreases.

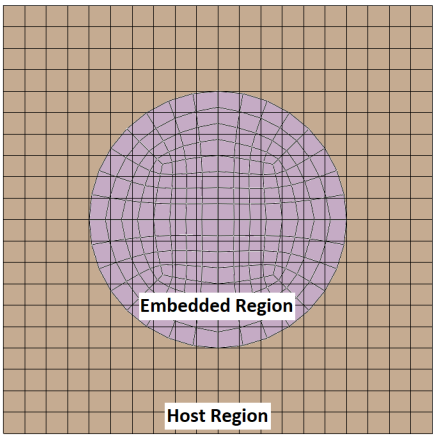


Figure 3.10: Illustrations of the embedded and host regions in a single inclusion RVE

The embedded region is superimposed onto the host region, as illustrated in Figure 3.10, which causes extra volume in the system. Ultimately, the system gains addi-

tional strain energy, which leads to changes in the total energy [33].

The EEM possesses some limitations, such as "rotational, electrical potential, pore or acoustic pressure, and temperature DOFs in the embedded region can not be constrained" [51]. In addition to that, the system gains additional mass and stiffness. However, this study does not contain elements with rotational DOF. Also, pressure, temperature, and electric potential DOFs are not concerned in this thesis. The determination of the mechanical properties in order to cope with the additional stiffness is studied and presented in Appendix A.

Figure 3.11 presents the flowchart for the computation of the homogenized elastic properties. This flowchart summarizes the work from the beginning to the end of the study. In the first step, particles are placed in the matrix randomly using the random sequential adsorption algorithm. After that, agglomerations are detected using a script written in Matlab. Material properties of the agglomerations are assigned using the inverse rule of mixture. Then, RVEs are created for the cases with and without agglomerations using the embedded element method. Average stress and strain values are computed using a script written in Python. The elasticity tensor is obtained using the average stress and strain values. Ultimately, elastic coefficients are calculated from the elasticity tensor.

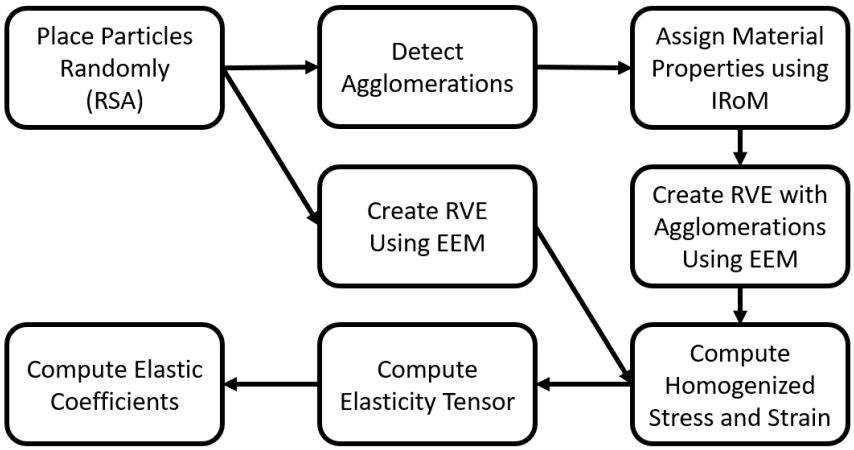


Figure 3.11: Flowchart for the computation of the homogenized mechanical properties

CHAPTER 4

NUMERICAL RESULTS

In this chapter, the numerical results of the various studies that are crucial in the appropriate modeling of the nanocomposite are presented, such as the convergence with mesh size and convergence with the number of particles. Besides, several comparison studies are presented, such as the comparison of the EEM and FEM, boundary conditions, and the results of the present study with the literature.

4.1 Convergence with Mesh Size

The quality of all discretization-based numerical methods depends on the fineness of the discretization used. Therefore, a mesh convergence study needed to be conducted to have realistic results by using the minimum number of nodes and elements. The RVE is constructed with solid elements containing three translational degrees of freedom in each node. Keeping the number of degrees of freedom low decreases the calculation time and necessary computer memory. Since the total number of finite element analyses is considerably high, keeping the duration of one analysis low is important.

For the mesh convergence study, an RVE with single inclusion is used. A particular ratio between the edge length of the RVE and the diameter of the inclusion is selected.

Since the performance of the embedded element meshing method is the main issue to check, a regular finite element method model with a regular finite element mesh is prepared. In the finite element model, which is taken as the reference, a spheri-

cal hole is partitioned, and inclusion is placed so that the nodes on both surfaces are overlapped. Besides this reference model, five different models are constructed using the embedded element method with various numbers of elements. The edge length of a model is prescribed as 1 unit, while the radius of the inclusion is 0.25. Therefore, the volume fraction is approximately 6.5%. Young's modulus of the matrix and the inclusions are prescribed as 3.7GPa and 1000GPa, respectively. Spherical inclusion is partitioned into eight parts to have a proper mesh with an aspect ratio near 1 and with similar element edge lengths. The value of the edge seed is fixed to 6 along the radius on the inclusion while the number of nodes along the matrix increases.

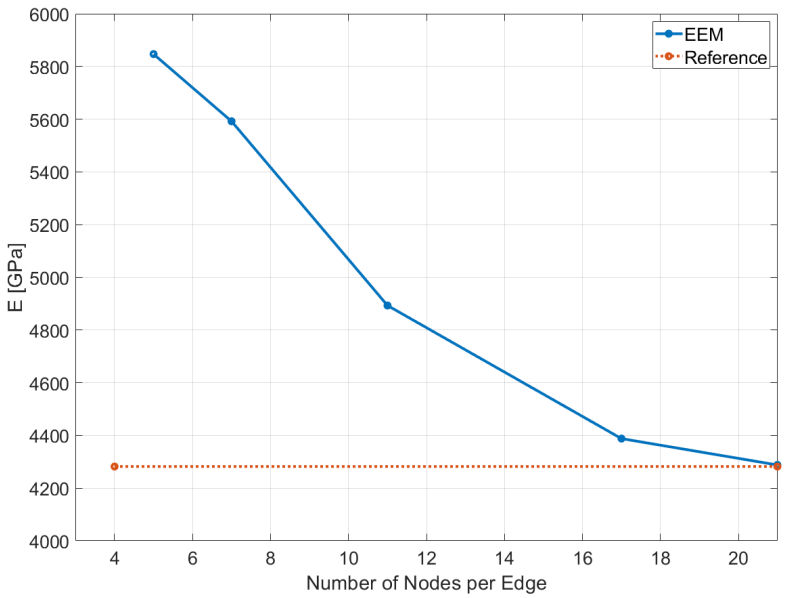


Figure 4.1: Results of the mesh convergence study of a single inclusion RVE with 6.5% volume fraction

Figure 4.1 and Table 4.1 help to decide the number of elements that should be chosen to obtain a precise result. According to Figure 4.1, the number of elements in the matrix should be at least 8000 as 21 nodes per edge. Therefore, the number of elements per edge is chosen as 20, and the total number of elements in the matrix is 8000 for a reliable model. Another mesh convergence study is conducted for the finite element

analysis result that is taken reference here. Finite element mesh is fine enough to be taken as a reference.

Table 4.1: Homogenized elastic modulus results of various mesh densities

Mesh Level	E [MPa]	# of Elements	# of Nodes
1	5847	320	446
2	5592	472	664
3	4893	768	1050
4	4388	4352	5234
5	4288	8356	9582
FEM	4282	57344	62083

The final discretization of the single inclusion model can be seen in Figure 4.2.

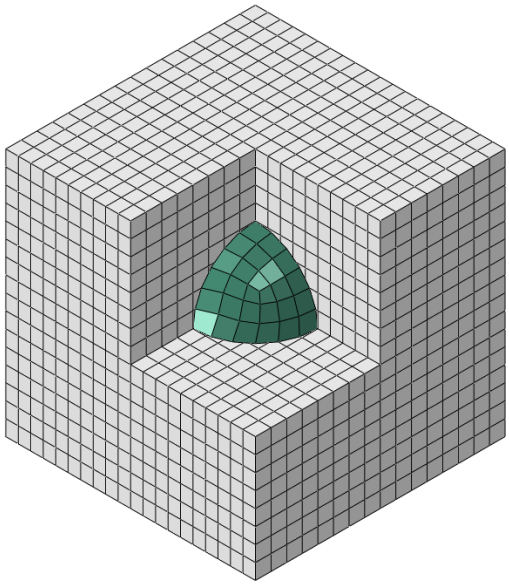


Figure 4.2: Illustration of the final discretization of a single inclusion RVE according to the results

4.2 Convergence with Number of Particles

Agglomeration formation is directly related to the number of particles in an RVE. For a decided volume fraction, if the size of the particles is large, the number of particles would be less. Therefore, the chance of agglomeration formation would be less. Regarding this phenomenon, the number of particles inside an RVE is crucial while investigating the aspects of the agglomeration on the mechanical properties of a nanocomposite.

In this study, five models are prepared to determine the minimum number of particles in an RVE. Models contain 1, 6, 12, 96, and 764 particles. All models contain a 5% volume fraction. The edge length of the RVE is kept the same in all models. The radius of particles is calculated as 2.285, 1.25, 1.0, 0.5, and 0.25 units, respectively. Two cases of analyses are conducted with the aforementioned models as well-dispersed particles and agglomerated particles. The elastic moduli of these cases are calculated and compared with each other to observe the agglomeration effect, as presented in Table 4.2 and Figure 4.3.

Table 4.2: Homogenized elastic modulus results of the five cases of the study of the convergence of the number of particles

# of Inclusion	E_{agg} [GPa]	E_{iso} [GPa]	Difference [%]
1	4.07	4.07	0.00
6	4.09	4.09	0.00
12	4.00	4.10	2.44
96	3.93	4.12	4.61
764	3.93	4.13	4.84

In the present study, the matrix's elastic modulus and Poisson ratio are taken as 3530MPa and 0.35, while these values are taken as 70GPa and 0.17 for inclusion. The mechanical properties of the materials are taken from the literature [65]. E_{agg} represents the elastic modulus of the case with agglomerations, while E_{iso} represents the well-dispersed particle case. E_{agg} and E_{iso} values are the average values of the

elastic moduli in three directions of three models with different random realizations of particles..

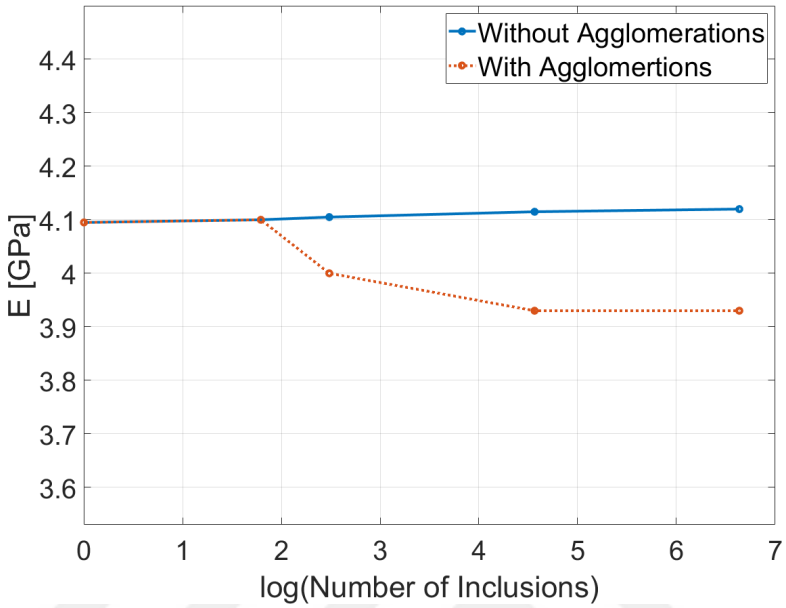
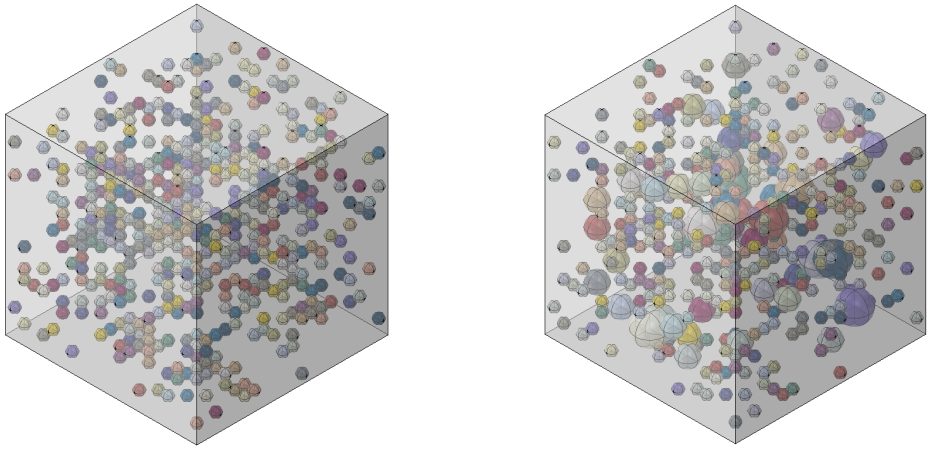


Figure 4.3: Results of the convergence of the number of particles study to observe the agglomeration effect with 5% volume fraction. The number of inclusions axis is on a logarithmic scale.

The line graph in Figure 4.3 helps to decide the minimum number of particles to catch the agglomeration effect. The blue line corresponds to the case without agglomeration, so it does not change much with the number of particles. The agglomeration effect can not be observed with the number of particles 1 and 6. There is a decrease in elastic modulus due to agglomerations after 12 particles. On the other hand, convergence is satisfied after 100 particles for a five percent volume fraction. In addition, for a lower volume fraction, since the number of inclusion would be less, the agglomeration effect would be harder to observe. Therefore, the radius of the particle is chosen as 0.25nm, while the edge length of the RVE is 10nm. The illustrations of the RVE with agglomerations and without agglomerations can be seen in Figure 4.4 for 5% of the volume fraction.



(a) RVE with well-dispersed particles

(b) RVE with agglomerated particles

Figure 4.4: Illustrations of the RVEs with (a) well-dispersed and (b) agglomerating particles for 125 numbers of particles with radius 0.25nm.

4.3 Comparison of EEM and FEM Results

The embedded element method and classical finite element method treat different the interaction between inclusion and matrix, which leads to differences in the results of the homogenized mechanical properties. On the other hand, the difference between results should not be too much if the model is created appropriately since both methods are used in practice, as elaborated in Chapter 2. Therefore, a comparison study is conducted between the two methods.

For this study, two RVEs are created with single inclusions. One of them is created as a standard finite element model, while the other one is created with an embedded region. The multi-inclusion model is not used for this study due to the high preprocessing cost. The elastic modulus of the inclusion is taken as 1000GPa, while it is 3700MPa for the matrix. Poisson ratios of the inclusion and the matrix are taken as 0.17 and 0.35, respectively. The comparison can be seen in Table 4.3 for a 1% volume fraction.

Table 4.3: Homogenized elastic modulus results of FEM and EEM

E_{FEM} [MPa]	E_{EEM} [MPa]	Difference [%]
3764.33	3800.52	0.96

The difference in the elastic modulus between the two methods is less than 1%. It gives an inference that the embedded element method does not give extraordinary results, therefore, can be used with the predetermined element size.

Another study is conducted to observe how different would be the elastic modulus of a multi-inclusion RVE than an RVE with single inclusion. For a 1% volume fraction, ten random realizations are generated, and homogenized properties are obtained. The elastic modulus in three directions is obtained and averaged using Equation 3.14.

Table 4.4: Average elastic modulus results of the RVEs with single inclusion and multi-inclusion

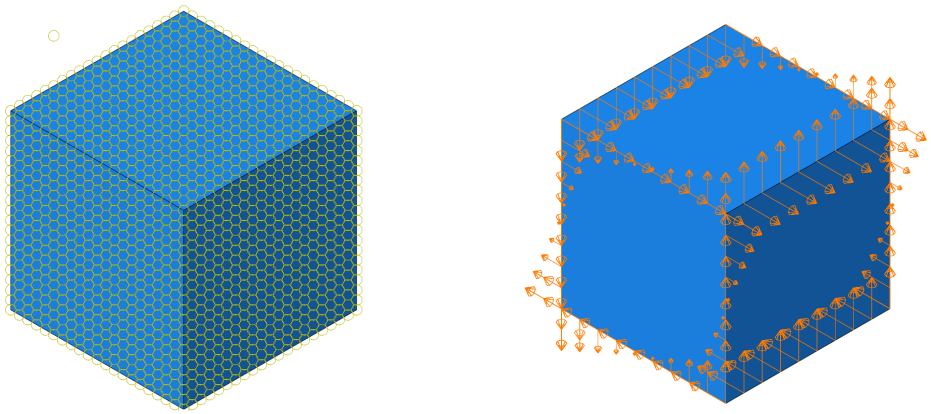
Analysis Number	E [MPa]	Difference wrt FEM [%]	Difference wrt EEM [%]
1	3966.21	5.36	4.36
2	3899.69	3.60	2.61
3	3933.06	4.48	3.49
4	3905.99	3.76	2.78
5	3946.82	4.85	3.85
6	3920.34	4.14	3.15
7	3905.21	3.74	2.75
8	3956.82	5.11	4.11
9	3920.34	4.14	3.15
10	3905.21	3.74	2.75

Table 4.4 shows the results of the differences between single-inclusion and multi-inclusion RVEs from ten different seeds. A little difference is expected, and the results are similar to each other. Therefore, if agglomeration is not to be modeled, RVEs with a single inclusion would be sufficient.

4.4 Comparison of Different Boundary Conditions

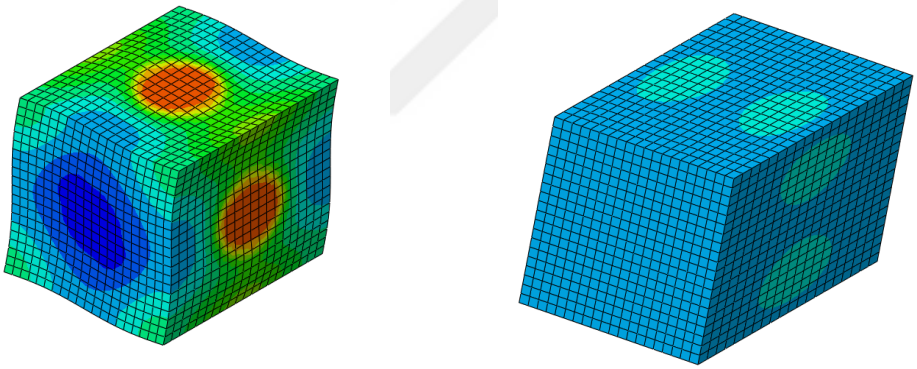
RVE size and inclusion size differ in this study significantly due to realistic modeling concerns. The matrix geometry contains many relatively small inclusions to reflect the agglomeration effect clearly. On the other hand, since the quality of the results in the embedded element method depends on the mesh size, matrix geometry is discretized into too many elements. In this scenario, using periodic boundary conditions is not very feasible. The output of the mesh density study results in 753571 nodes on the matrix only. This number decreases to 24843 nodes on the surfaces of the matrix, which need to be constrained in three degrees of freedom. Therefore, in total, 72096 constraint equations would be added to the model. Even applying the PBC before running the simulation increases computational costs excessively. However, a comparison study between the two methods is conducted to validate the results of the uniform displacement boundary condition.

Due to the reasons that are stated above, a single-inclusion RVE is chosen to apply both boundary condition types, as illustrated in Figure 4.5. PBC is applied using a script. The script constrains each degree of freedom of a node to that specific degree of freedom of a node on the exact opposite side [61]. The displacement-driven test in whichever direction would be satisfied by changing the value of that degree of freedom in relevant surface nodes. On the other hand, in DBC, the boundary condition is applied directly to the nodes on the relevant surfaces in opposite directions while restricting other surface nodes in uniaxial tensile test.



(a) Periodic boundary condition in shear load (b) Displacement boundary condition in shear load

Figure 4.5: Illustrations of the application of (a) periodic boundary conditions and (b) linear displacement boundary conditions



(a) Shear load result with PBC (b) Shear load result with DBC

Figure 4.6: Illustrations of deformed RVEs with (a) periodic boundary conditions and (b) displacement boundary conditions applied under shear load

Homogenized elastic and shear modulus results are calculated using both types of boundary conditions. The elastic moduli of matrix and inclusion are taken as 3530MPa and 70GPa, while Poisson ratios are 0.35 and 0.17, respectively.

Table 4.5: Comparison of homogenized elastic constants results with DBC and PBC

Property	E [MPa]	G [MPa]
PBC	4080.26	1483.90
DBC	4107.49	1521.45
Difference [%]	0.66	2.08

The difference in the deformed shapes after the application of the shear load is illustrated in Figure 4.6. The results and differences that are shown in Table 4.5 state that the DBC can be replaced with PBC in multi-inclusion RVE since the application of the PBC is infeasible.

4.5 Homogenized Elastic Constants

The homogenized mechanical properties of the nanocomposite are calculated for both agglomerated particles case and the well-dispersed particles case. A degradation in mechanical properties is mentioned in Chapter 2 with agglomerating particles. Material properties are acquired from Demir et al. [8], and the volume fraction is taken as 2%. Young's modulus of the particle is taken as 1000GPa, as 911MPa for the matrix. Poisson's ratios are taken as 0.35 for all three phases. There are 306 randomly distributed particles with a size of 0.5nm in the RVE. The degradation in Young's and shear moduli due to agglomerations can be observed in Tables 4.6 and 4.7.

Table 4.6: Homogenized elastic modulus results of the nanocomposite

	E_x [MPa]	E_y [MPa]	E_z [MPa]
No Agglomeration	1030.14	1019.37	1021.25
Agglomeration	1009.09	1004.04	1003.37
Difference [%]	2.26	1.50	1.75

Table 4.7: Homogenized shear modulus results of the nanocomposite

	G_{yz} [MPa]	G_{xz} [MPa]	G_{xy} [MPa]
No Agglomeration	382.72	380.71	382.36
Agglomeration	372.68	375.61	374.52
Difference [%]	2.62	1.34	2.05

The upper bound (Voigt) of the elastic modulus of the RVE is calculated as 3892.78MPa, and the lower bound (Reuss) is calculated as 929.48MPa. Due to the spherical geometry of the inclusion, the results, as expected, are close to the lower bound.

4.6 Comparison with Experiments

The presented study shows a decrease in the elastic modulus of the composite after a limit of the volume fraction. In literature, similar effects are observed, as elaborated in Chapter 2. The critical volume fraction varies with the particle's radius, surface treatment, or functionalized particles. By following the procedure detailed in Chapter 3, an RVE is created to compare the results of the present study with the results of the experiment [28]. Material properties are taken from the article. Linear low-density polyethylene is used as the matrix with Young's modulus of 51MPa, and silica Aerosil R972 is used as filler with 70GPa elastic modulus. The Poisson's ratios for the matrix and the particle are taken as 0.35 and 0.17, respectively. The specific surface of the particle is $130m^2/g$, and the average particle size is 16nm.

Five different percentages of loading, 2, 4, 6, 8, and 10%, are used in the experiment. Three critical distance values are considered in simulations, and Young's modulus versus volume fraction relations are plotted. Note that the critical distance is the distance between the centers of two particles. Besides, Voigt and Reuss bounds are also included in the line graph with well-dispersed particle case results.

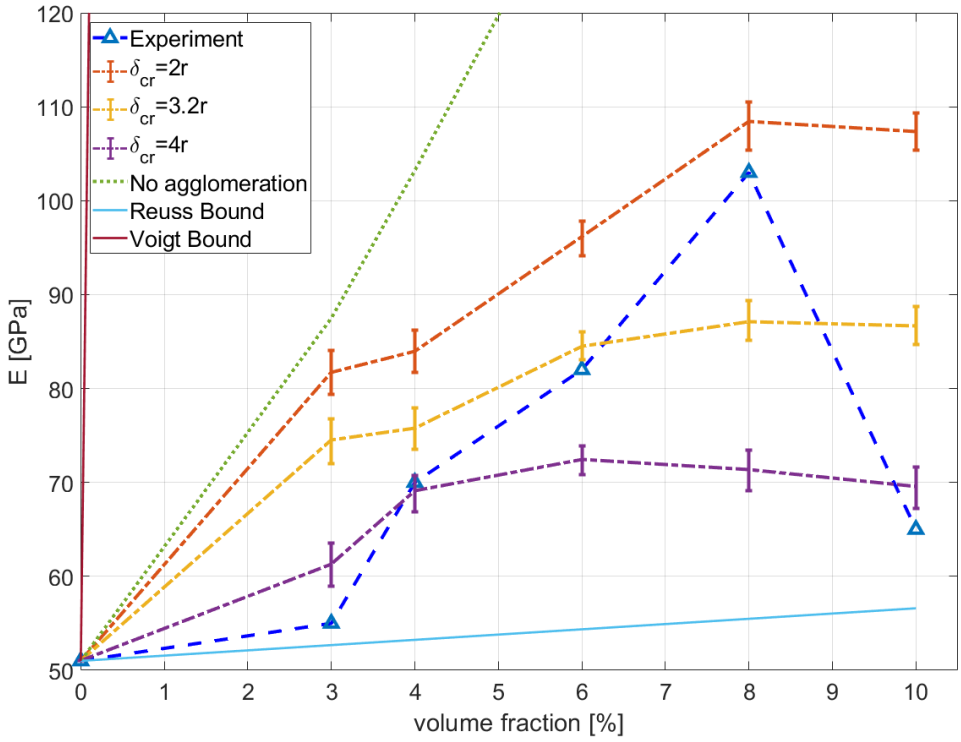


Figure 4.7: Comparison of the results of the present study with the experiment

In this comparison study, numerical results show a similar trend to the experiment; see Figure 4.7. After an 8% volume fraction, a decrease in elastic modulus value is observed. In the results of the largest critical distance case, the decrease begins after 6% since the volume fraction of the agglomeration phases increases more. On the other hand, the decrease level is more drastic in the experiment. As expected, both experimental and numerical results are inside the range of Reuss and Voigt bounds. Additionally, a linear increase is observed in the case with no agglomerations. All numerical results of elastic modulus are averaged in each direction for three different random seeds, as stated in Equation 3.14.

Table 4.8 puts forward that the number of free particles decreases after 8% when $\delta_{cr} = 2r$ and $\delta_{cr} = 3.2r$, and 6% volume fraction filler loading when $\delta_{cr} = 4r$. The reason behind the decrease in the elastic modulus in Figure 4.7 depends on the decrease in the number of free particles. The number of clusters does not increase with

the increasing volume fraction since the clusters of two particles become the clusters of three and four particles with the increasing volume fraction. Therefore, the number of clusters of two particles decreases while the number of clusters of three and four particles increases. The mechanical properties of the clusters are similar to the matrix, slightly larger than the matrix. Therefore, the main reinforcement mechanism is provided by the free particles. This phenomenon can be observed when the critical distance increases to 4r at the 6% volume fraction of filler, as can be seen in Table 4.8.

Table 4.8: Variation of the cluster numbers with volume fractions and critical distance

δ_{cr}	v_f [%]	# of Particles	# of Free Particles	# of Clusters
2r	3	460	341	42
	4	611	412	56
	6	916	565	82
	8	1222	647	89
	10	1528	618	99
3.2r	3	460	218	43
	4	611	236	39
	6	916	271	49
	8	1222	314	41
	10	1528	292	39
4r	3	460	71	20
	4	611	127	14
	6	916	141	16
	8	1222	119	12
	10	1528	108	18

The agglomeration density decreases with the increasing particle radius. The specific surface (the surface area per unit mass) and the agglomeration density are inversely re-

lated. To this end, another comparison study is conducted with three different particle radii to observe such a phenomenon. The mechanical properties are taken from [65], and the experimental results are used to compare the numerical results. The matrix material is taken as bis-phenol A epoxy resin, and silica Aerosil 200, Aerosil 90, and Aerosil OX50 are used as particles. The average particle sizes are 12, 20, and 40nm. The specific surfaces of the particles are 200, 90, and $50 m^2/g$, respectively. The elastic modulus of the matrix and the particles are taken as 3530MPa and 70GPa, and the Poisson's ratios are taken as 0.35 and 0.17, respectively. To represent different particle radii, different critical values are taken into account. For the experimental result of the case with the smallest particles (12nm), a relatively large critical distance (4r) is chosen, while for the case with the largest particles (40nm), a small critical distance (2r) is used. The numerical results are plotted with the results of the experiments in Figure 4.8-4.10. Three random realizations of particles are examined, and the elastic moduli in three directions of each realization are averaged, as explained in Equation 3.14. The maximum and minimum results for each volume fraction are shown in the figures. Also, the analytical results of Voigt and Reuss bounds are added in figures as well as the results of the well-dispersed particles case.

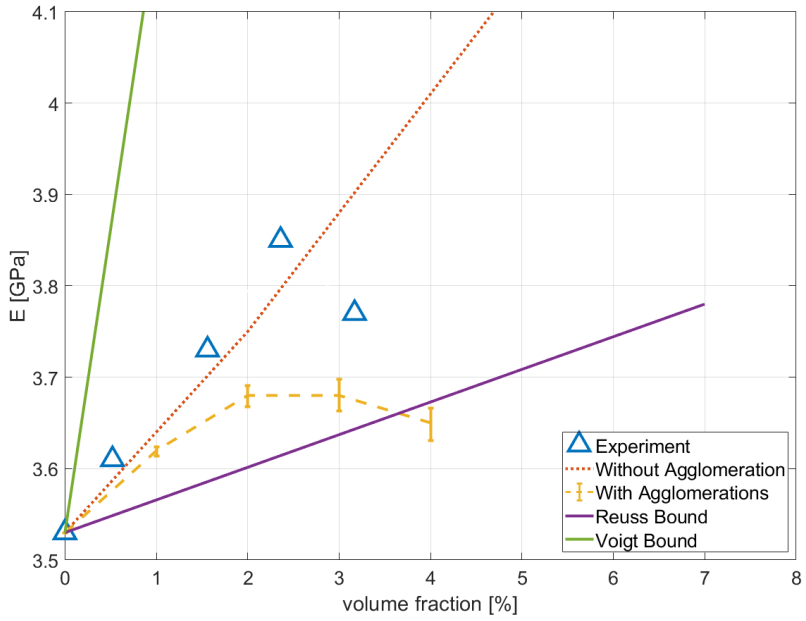


Figure 4.8: Comparison of the results with experiment with 12nm particle size while $\delta_{cr} = 4r$

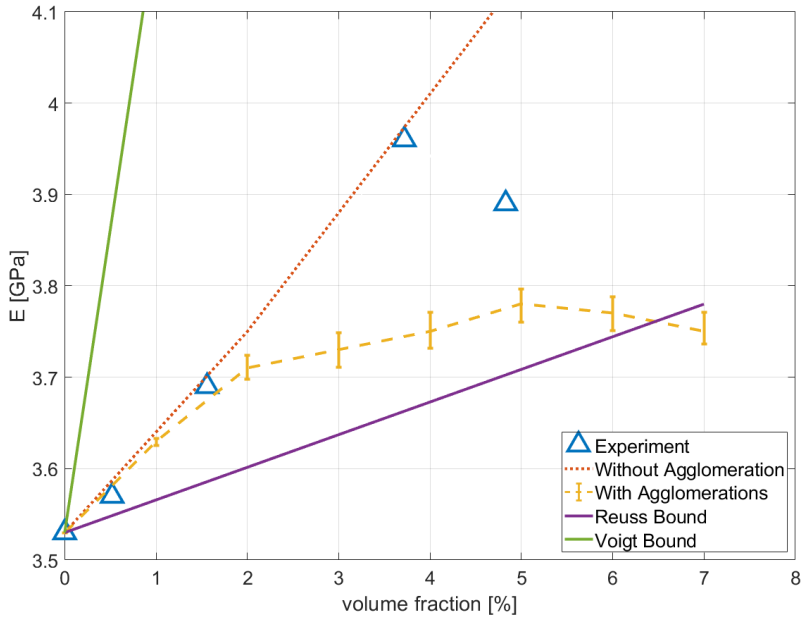


Figure 4.9: Comparison of the results with experiment with 20nm particle size while $\delta_{cr} = 3.2r$

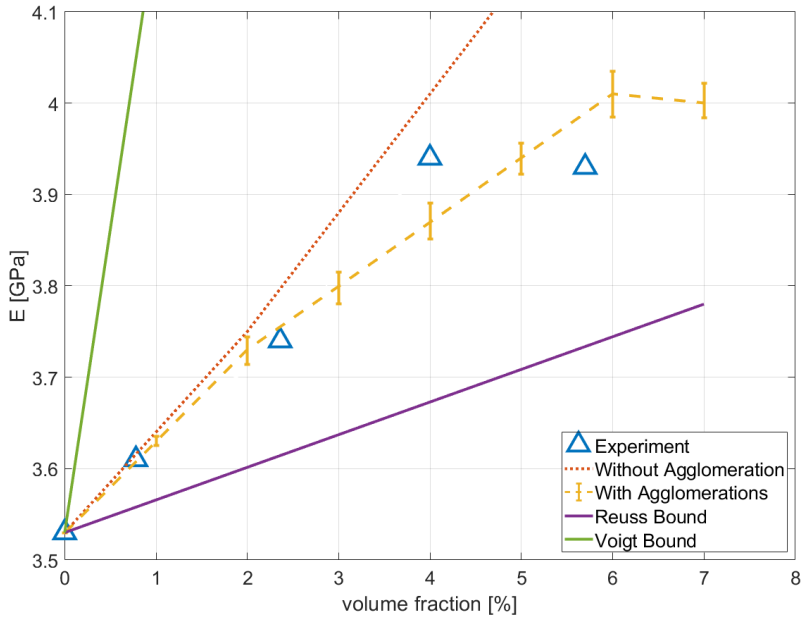


Figure 4.10: Comparison of the results with experiment with 40nm particle size while $\delta_{cr} = 2r$

Figures 4.8-4.10 show that the experimental and numerical results show similar trends. After specific volume fractions, a decrease in elastic modulus is observed. Simulations without the effect of the agglomerations show a linear increase in elastic modulus for each model, as expected. Also, both the experimental and numerical results are inside the range of Voigt and Reuss bounds.

A consequence of the different particle sizes can be seen in the varying critical volume fraction before degradation. Figure 4.8 shows that the degradation in the elastic properties begins after 2.5% filler loading, while the degradation begins after 5% filler loading in Figure 4.10. The specific surface increases with the decreasing particle size. Therefore, this ends up with more tendency in particles to agglomerate. In the end, the degradation aspect of the agglomeration can be seen earlier in the particles with higher specific surfaces and smaller sizes. This phenomenon can be observed in Figures 4.8-4.10.

CHAPTER 5

CONCLUSION

In the thesis, a nonhomogenous nanocomposite with spherical inclusions is homogenized using the embedded element method. Some simplifications and idealizations are employed to simulate the response of the nanocomposite while easing the computational process. Firstly, the random sequential adsorption (RSA) algorithm is employed to simulate the random dispersion of the particles. Then, to decrease the computational effort, an RVE is created to represent the same mechanical properties of the nanocomposite. The embedded element method is also used to ease the preprocessing effort. Ultimately, to extract the elastic constants of the material, a script is written in Python in the homogenization step.

Most homogenization techniques need to be revised to calculate the material properties precisely. Analytical homogenization methods mostly do not include the interaction between the particle and the matrix or assume the distribution of the fillers as uniform and aligned. On the other hand, in nanocomposites, particles tend to agglomerate, which leads to a degradation in the mechanical properties. In this thesis, the effect of agglomeration on elastic properties is examined. The results show a decrease in elastic modulus after a critical volume fraction. On the other hand, homogenization would obtain only a linear increase of elastic properties with the volume fraction of inclusion if the agglomeration effect is not taken into account.

The RVE size is a crucial point to include the agglomeration effect. The number of particles in an RVE directly affects the clustering density. A study is conducted to find the minimum number of inclusions needed to represent the agglomeration effect properly. According to the results, the optimum RVE size and the number of inclu-

sions are obtained.

The embedded and finite element methods are compared by homogenizing a single inclusion RVE. In order to make a fair comparison, a mesh convergence study is conducted for both cases. The homogenized mechanical properties differ by less than 1%. Therefore, the use of the EEM is decided to be convenient.

Generally, periodic boundary conditions (PBC) are preferred while analyzing an RVE of a whole composite. In the thesis, PBC is applied to an RVE with a single inclusion. However, applying PBC to the RVE with multiple inclusions is not feasible due to the number of nodes per surface predetermined by the mesh convergence study. Therefore, the results of the model with linear displacement boundary conditions (DBC) are compared with those of the model with PBC. Since the results are compatible, DBC is applied in the multi-inclusion model.

Ultimately, two studies from the literature are chosen to compare the homogenized elastic modulus results. These studies use silica-based nanoparticles and contain experimental results. Experimental results show a decrease in the elastic modulus at some volume fraction, and the numerical results calculated in this thesis are coherent. Besides, it is observed that the size of the particle is a prominent factor in the agglomeration effect. The clustering density increases with the increase in the specific surface of the particles.

This study can also be extended to include the effect of the interphase. The effect of the interphase is studied in the literature, and a more precise study can be conducted. Additionally, some applications may be enhanced in this thesis. Firstly, an algorithm to create an RVE with the sliced particles on the surfaces can be developed. In this study, particles are placed only inside the RVE. Then, an enhanced random dispersion algorithm can be developed instead of prescribing the possible coordinates of the particles.

The sizes of the agglomerations can be determined by obeying mass conservation instead of placing the smallest sphere that encapsulates vanished particles. The den-

sity of the agglomerations can be used to determine the size of the agglomerations. The mechanical properties of the agglomerations can also be determined using the nano-indentation technique. There are several studies in the literature that employ the nano-indentation method to obtain the local elastic properties of composite materials. Besides, this method can be used in modulus mapping and determination of the interphase properties as well as the characterization of the polymer nanocomposites [24, 31, 45, 49, 57].

The degradation mechanism can be simulated by weakening the load transfer on the contact surfaces of the agglomerated particles. The degradation mechanism can be investigated by researching the damage mechanisms of the nanocomposite with agglomerations. Finally, the studies can be extended to include other types of inclusions, such as platelets and fibers.

REFERENCES

[1] A. E. Altay. Determination of elastic properties of polymer nanocomposites using embedded element method. Master's thesis, Middle East Technical University, 2022.

[2] M. A. Ashraf, W. Peng, Y. Zare, and K. Y. Rhee. Effects of size and aggregation/agglomeration of nanoparticles on the interfacial/interphase properties and tensile strength of polymer nanocomposites. *Nanoscale Research Letters*, 13(214), 2018.

[3] K. Baek, H. Shin, T. Yoo, and M. Cho. Two-step multiscale homogenization for mechanical behaviour of polymeric nanocomposites with nanoparticulate agglomerations. *Composites Science and Technology*, 179:97–105, 2019.

[4] H. Berger, S. Kari, U. Gabbert, R. Rodriguez-Ramos, R. Guinovart, J. A. Otero, and J. Bravo-Castillero. An analytical and numerical approach for calculating effective material coefficients of piezoelectric fiber composites. *International Journal of Solids and Structures*, 42(21-22):5692–5714, 2005.

[5] D. N. Bikiaris, A. Vassiliou, E. Pavlidou, and G. P. Karayannidis. Compatibilisation effect of pp-g-ma copolymer on ipp/sio2 nanocomposites prepared by melt mixing. *European Polymer Journal*, 41(9):1965–1978, 2005.

[6] H. J. Böhm. A short introduction to basic aspects of continuum micromechanics. *Cdl-fmd report*, 3, 1998.

[7] J. Chen, Y. Yu, J. Chen, H. Li, J. Ji, and D. Liu. Chemical modification of palygorskite with maleic anhydride modified polypropylene: Mechanical properties, morphology, and crystal structure of palygorskite/polypropylene nanocomposites. *Applied Clay Science*, 115:230–237, 2015.

[8] E. C. Demir, A. Benkaddour, D. R. Aldrich, M. T. McDermott, C. I. Kim, and C. Ayranci. A predictive model towards understanding the effect of reinforce-

ment agglomeration on the stiffness of nanocomposites. *Journal of Composite Materials*, 56/10:1591–1604, 2022.

[9] A. Dorigato, Y. Dzenis, and A. Pegoretti. Filler aggregation as a reinforcement mechanism in polymer nanocomposites. *Mechanics of Materials*, 61:79–90, 2013.

[10] F. Ebrahimi and A. Dabbagh. *Mechanics of nanocomposites homogenization and analysis*. CRC Press, 2020.

[11] J. A. Fankhänel. *A Multi-Scale Framework for Nanocomposites including Interphase and Agglomeration Effects*. PhD thesis, Gottfried Wilhelm Leibniz Universität, 2020.

[12] S. Firooz, S. Saeb, G. Chatzigeorgiou, F. Meraghni, P. Steinmann, and A. Javili. Systematic study of homogenization and the utility of circular simplified representative volume element. *Mathematics and Mechanics of Solids*, 24(9):2961–2985, 2019.

[13] H. T. Garimella, R. R. Menghani, J. I. Gerber, S. Sridhar, and R. H. Kraft. Embedded finite elements for modeling axonal injury. *Annals of Biomedical Engineering*, 47:1889–1907, 2019.

[14] I. Gosens, J. A. Post, L. J. de la Fonteyne, E. H. Jansen, J. W. Geus, F. R. Cassee, and W. H. de Jong. Impact of agglomeration state of nano-and submicron sized gold particles on pulmonary inflammation. *Particle and Fibre Toxicology*, 7(1):1–11, 2010.

[15] H. Gu, Y. Guo, S. Y. Wong, C. He, X. Li, and V. Shim. Effect of interphase and strain-rate on the tensile properties of polyamide 6 reinforced with functionalized silica nanoparticles. *Composites Science and Technology*, 75:62–69, 2013.

[16] D. Güzel. A two-level homogenization method for polymer nancomposites with coated inclusions. Master's thesis, Middle East Technical University, 2019.

[17] D. Güzel and E. Gürses. A two-level homogenization approach for polymer nanocomposites with coated inclusions. *Procedia Structural Integrity*, 35:34–41, 2022.

[18] A. Hančič, F. Kosel, K. Kuzman, and J. M. Slabe. Comparison of two micromechanical models for predicting elasto-plastic response of wood–plastic composites. *Composites Part B: Engineering*, 43(3):1500–1507, 2012.

[19] Z. Hashin and S. Shtrikman. A variational approach to the theory of the elastic behaviour of multiphase materials. *Journal of the Mechanics and Physics of Solids*, 11(2):127–140, 1963.

[20] S. Hazanov. Hill condition and overall properties of composites. *Archive of Applied Mechanics*, 68(6):385–394, 1998.

[21] S. Hazanov and M. Amieur. On overall properties of elastic heterogeneous bodies smaller than the representative volume. *International Journal of Engineering Science*, 33(9):1289–1301, 1995.

[22] R. Hill. Elastic properties of reinforced solids: some theoretical principles. *Journal of the Mechanics and Physics of Solids*, 11(5):357–372, 1963.

[23] S. Kareem, L. S. Al-Ansari, and L. A. Gömze. Modeling of modulus of elasticity of nano-composite materials: review and evaluation. In *Journal of Physics: Conference Series*, volume 2315, page 012038. IOP Publishing, 2022.

[24] A. Karimzadeh, S. R. Koloor, M. R. Ayatollahi, A. R. Bushroa, and M. Y. Yahya. Assessment of nano-indentation method in mechanical characterization of heterogeneous nanocomposite materials using experimental and computational approaches. *Scientific reports*, 9(1):15763, 2019.

[25] G. Keledi, J. Hári, and B. Pukánszky. Polymer nanocomposites: structure, interaction, and functionality. *Nanoscale*, 4(6):1919–1938, 2012.

[26] A. Khan, M. H. Shamsi, and T. S. Choi. Correlating dynamical mechanical properties with temperature and clay composition of polymer-clay nanocomposites. *Computational Materials Science*, 45(2):257–265, 2009.

[27] I. Khan, K. Saeed, and I. Khan. Nanoparticles: Properties, applications and toxicities. *Arabian Journal of Chemistry*, 12(7):908–931, 2019.

[28] E. Kontou and M. Niaounakis. Thermo-mechanical properties of lldpe/sio2 nanocomposites. *Polymer*, 47:1267–1280, 2006.

[29] M. Kurt. Numerical calculation of homogenized properties of piezoelectric composites. Master's thesis, Middle East Technical University, 2022.

[30] R. S. Lakes. *Viscoelastic materials*. Cambridge university press, 2009.

[31] C. K. Lam and K. T. Lau. Localized elastic modulus distribution of nanoclay/epoxy composites by using nanoindentation. *Composite structures*, 75(1-4):553–558, 2006.

[32] H. Liu, D. Zeng, Y. Li, and L. Jiang. Development of rve-embedded solid elements model for predicting effective elastic constants of discontinuous fiber reinforced composites. *Mechanics of Materials*, 93:109–123, 2016.

[33] V. A. Martin, R. H. Kraft, T. H. Hannah, and S. Ellis. An energy-based study of the embedded element method for explicit dynamics. *Advanced Modeling and Simulation in Engineering Sciences*, 9(1):1–18, 2022.

[34] A. Matveeva, V. Romanov, S. Lomov, and L. Gorbatikh. Application of the embedded element technique to the modelling of nano-engineered fiber-reinforced composites. In *Proceedings of the ICCM International Conferences on Composite Materials, Copenhagen, Denmark*, pages 19–24, 2015.

[35] J. V. Milewski. Whiskers and short fiber technology. *Polymer Composites*, 13(3):223–236, 1992.

[36] T. Mori and K. Tanaka. Average stress in matrix and average elastic energy of materials with misfitting inclusions. *Acta Metallurgica*, 21(5):571–574, 1973.

[37] M. Mu, E. Teblum, Ł. Figiel, G. D. Nessim, and T. McNally. Correlation between mwcnt aspect ratio and the mechanical properties of composites of pmma and mwcnts. *Materials Research Express*, 5(4):045305, 2018.

[38] V. P. Nguyen. Scales bridging in material modelling a review on computational homogenisation techniques. 2009.

[39] S. L. Omairey, P. D. Dunning, and S. Sriramula. Development of an abaqus plugin tool for periodic rve homogenisation. *Engineering with Computers*, 35:567–577, 2018.

[40] M. Ostoja-Starzewski. Material spatial randomness: From statistical to representative volume element. *Probabilistic Engineering Mechanics*, 21(2):112–132, 2006.

[41] D. H. Pahr and H. J. Böhm. Assessment of mixed uniform boundary conditions for predicting the mechanical behavior of elastic and inelastic discontinuously reinforced composites. *Computer Modeling in Engineering Science*, 34:117–136, 2008.

[42] B. Pal and M. R. Haseebuddin. Analytical estimation of elastic properties of polypropylene fiber matrix composite by finite element analysis. *Advances in Materials Physics and Chemistry*, 2:23–30, 2012.

[43] A. Pontefisso, M. Zappalorto, and M. Quaresimin. An efficient rve formulation for the analysis of the elastic properties of spherical nanoparticle reinforced polymers. *Computational Materials Science*, 96:319–326, 2015.

[44] P. Qian, Q. Xu, et al. Development of embedded element technique for permeability analysis of cracked porous media. *Mathematical Problems in Engineering*, 2017, 2017.

[45] Y. Raichman, M. Kazakevich, E. Rabkin, and Y. Tsur. Inter-nanoparticle bonds in agglomerates studied by nanoindentation. *Advanced Materials*, 18(15):2028–2030, 2006.

[46] A. Reuss. Berechnung der fließgrenze von mischkristallen auf grund der plastizitätsbedingung für einkristalle . *ZAMM - Journal of Applied Mathematics and Mechanics / Zeitschrift für Angewandte Mathematik und Mechanik*, 9(1):49–58, 1929.

[47] Y. Rémond, S. Ahzi, M. Baniassadi, and H. Garmestani. *Applied RVE reconstruction and homogenization of heterogeneous materials*. Wiley Online Library, 2016.

[48] S. Saeb, P. Steinmann, and A. Javili. Aspects of computational homogenization at finite deformations: a unifying review from Reuss' to Voigt's bound. *Applied Mechanics Reviews*, 68(5):050801, 2016.

[49] M. Sánchez, J. Rams, M. Campo, A. Jiménez-Suárez, and A. Ureña. Characterization of carbon nanofiber/epoxy nanocomposites by the nanoindentation technique. *Composites Part B: Engineering*, 42(4):638–644, 2011.

[50] H. Shin, S. Yang, J. Choi, S. Chang, and M. Cho. Effect of interphase percolation on mechanical behavior of nanoparticle-reinforced polymer nanocomposite with filler agglomeration: A multiscale approach. *Chemical Physics Letters*, 635:80–85, 2015.

[51] D. S. Simulia. Abaqus 6.12 analysis user's manual providence. *RI, USA*, 2012.

[52] P. Suquet. Elements of homogenization for inelastic solid mechanics. *Homogenization Techniques for Composite Media*, 1987.

[53] S. A. Tabatabaei and S. Lomov. Eliminating the volume redundancy of embedded elements and yarn interpenetrations in meso-finite element modelling of textile composites. *Computers and Structures*, 152:142–154, 2015.

[54] S. A. Tabatabaei, S. Lomov, and I. Verpoest. Assessment of embedded element technique in meso-fe modelling of fibre reinforced composites. *Composite Structures*, 107:436–446, 2014.

[55] S. A. Tabatabaei and S. V. Lomov. Embedded element method in meso finite element modelling of textile composites: "a gallery". In *ICCM International Conferences on Composite Materials*, 07 2015.

[56] S. Torquato. *Random heterogeneous materials microstructure and macroscopic properties*. Springer Link, 2002.

[57] P. Uskokovic, C. Y. Tang, C. P. Tsui, N. Ignjatovic, and D. Uskokovic. Micromechanical properties of a hydroxyapatite/poly-l-lactide biocomposite using nanoindentation and modulus mapping. *Journal of the European Ceramic Society*, 27(2-3):1559–1564, 2007.

[58] W. Voigt. Lehrbuch der kristallphysik. *Teubner, Leipzig*, 1928.

[59] B. Widom. Random sequential addition of hard spheres to a volume. *The Journal of Chemical Physics*, 44(10):3888–3894, 1966.

[60] D. Wu, L. Wu, W. Zhou, Y. Sun, and M. Zhang. Relations between the aspect ratio of carbon nanotubes and the formation of percolation networks in biodegradable polylactide/carbon nanotube composites. *Journal of Polymer Science Part B: Polymer Physics*, 48(4):479–489, 2010.

[61] W. Wu, J. Owino, A. Al-Ostaz, and L. Cai. Applying periodic boundary conditions in finite element analysis. *2014 SIMULIA Community Conference*, 2014.

[62] X.-L. Xie, Q.-X. Liu, R. K.-Y. Li, X.-P. Zhou, Q.-X. Zhang, Z.-Z. Yu, and Y.-W. Mai. Rheological and mechanical properties of pvc/caco3 nanocomposites prepared by in situ polymerization. *Polymer*, 45(19):6665–6673, 2004.

[63] G. Zaikov, G. Kozlov, A. Mikitaev, O. Stoyanov, et al. The structural analysis of particulate-filled polymer nanocomposites mechanical properties. , 18(2):187–194, 2015.

[64] M. Zamanian, F. A. Ghasemi, and M. Mortezaei. Interphase characterization and modeling of tensile modulus in epoxy/silica nanocomposites. *Journal of Applied Polymer Science*, 138, 2020.

[65] M. Zamanian, M. Mortezaei, B. Salehnia, and J. E. Jam. Fracture toughness of epoxy polymer modified with nanosilica particles: Particle size effect. *Engineering Fracture Mechanics*, 97:193–206, 2013.

[66] Y. Zare. Study of nanoparticles aggregation/agglomeration in polymer particulate nanocomposites by mechanical properties. *Composites Part A: Applied Science and Manufacturing*, 84:158–164, 2016.

[67] Y. Zare, K. Y. Rhee, and D. Hui. Influences of nanoparticles aggregation/agglomeration on the interfacial/interphase and tensile properties of nanocomposites. *Composites Part B*, 122:41–46, 2017.

[68] G. Zhang and S. Torquato. Precise algorithm to generate random sequential addition of hard hyperspheres at saturation. *Physical Review E*, 88(5):053312, 2013.

[69] J. Zhou, L. Qi, and A. M. Gokhale. Generation of three-dimensional microstructure model for discontinuously reinforced composite by modified random se-

quential absorption method. *Journal of Engineering Materials and Technology*, 138(2):021001, 2016.

[70] A. Şık, E. Gürses, and B. Sabuncuoglu. Development of a procedure to model the mechanical behavior of composites with embedded element method by considering the matrix non-linearity. *Composite Structures*, 259:142–154, 2021.

Appendix A

The embedded elements add extra stiffness and mass to the system [51]. Therefore, in practice, a subtraction of the value of the elastic modulus of the matrix from the elastic modulus of the inclusion is performed.

$$E_{corrected} = E_i - E_m, \tag{A.1}$$

where E_i and E_m are the elastic modulus of the inclusion and the matrix, respectively.

In the problems analyzed, the mismatch of the elastic modulus between agglomerations and matrix is low, while this mismatch is high for the free particles and matrix. Therefore, a study is conducted to compare the errors of two cases, with subtraction and without subtraction. $E_{corrected}$ is assigned to the inclusion in the case with correction, while E_i is assigned to the inclusion in the case without correction. In both cases, 2 RVEs are created with only one inclusion with a 5% volume fraction with FEM and EEM. The material properties are chosen to observe the effect of the mismatch on the difference. Young's modulus of the matrix is chosen as 1000MPa while the elastic modulus of the inclusion is varied between 1000MPa to 100000MPa. Four cases are created with different levels of elastic modulus mismatch. The homogenized Young's modulus values of FEM and EEM are compared. The results are tabulated in Table A.1.

Table A.1: Comparison of the cases with and without correction

E_m [MPa]	E_i [MPa]	E_{EEM} [MPa] without correction	E_{EEM} [MPa] with correction	E_{FEM} $[MPa]$
1000	1000	1000.78	952.57	999.97
1000	2000	1027.50	1000.78	1034.68
1000	10000	1088.22	1085.18	1091.34
1000	100000	1120.32	1120.27	1112.19

The difference between the FEM and EEM results is acceptable when the mismatch between elastic modulus is high. Conversely, while the elastic modulus of the inclusion is similar to the matrix, the error is much larger. This table shows that the correction in the elastic modulus results in a higher error when the mismatch is low between the elastic modulus of the inclusion and the matrix. Therefore, subtraction is not performed while assigning the material properties of the agglomerations.

Appendix B

There will be 2 scripts in Appendix B that is employed in the thesis. First script is the homogenization script for the case with 125 randomly distributed particles with no agglomerations. Second script is used for the implementation of the periodic boundary conditions.

Listing B.1: Homogenization script written in Python for 125 particles

```
import time
starttime = time.time()
sums11 = 0.0 ; sums22 = 0.0; sums33 = 0.0
sums23 = 0.0; sums13 = 0.0; sums12 = 0.0
sume11 = 0.0 ; sume22 = 0.0; sume33 = 0.0
sume23 = 0.0; sume13 = 0.0; sume12 = 0.0
sumivol = 0.0

sums111 = 0.0; sums221 = 0.0; sums331 = 0.0
sums231 = 0.0; sums131 = 0.0; sums121 = 0.0
sume111 = 0.0; sume221 = 0.0; sume331 = 0.0
sume231 = 0.0; sume131 = 0.0; sume121 = 0.0
sumivol1 = 0.0

import sys, getopt, os, string
import math
from odbAccess import
from abaqusConstants import
odbPath =  simulationname.odb
odb = session.openOdb(name=odbPath,readOnly=FALSE)
keys = odb.steps.keys()
```

```
for i in range (125, 0,  1):
    for adim in keys:
        step = odb.steps[adim]
          retrieve frames from the odb
        frameRepository = step.frames
        numFrames = len(frameRepository)
        for decre in range (numFrames, numFrames 1,  1):
                grout instance1 = odb.rootAssembly.instances[ FIBER  + str(i 1) +  1 ]

                frame=step.frames[1]

                S = frame.fieldOutputs[ S ]
                E = frame.fieldOutputs[ E ]
                IVOL = frame.fieldOutputs[ IVOL ]
                S grout = S.getSubset(region=grout instance1 ,
                position=INTEGRATIONPOINT,
                elementType= C3D8 )
                E grout = E.getSubset(region=grout instance1 ,
                position=INTEGRATIONPOINT,
                elementType= C3D8 )
                IVOL grout = IVOL.getSubset(region=grout instance1 ,
                position=INTEGRATIONPOINT,
                elementType= C3D8 )

                sums11 += 0.0
                sums22 += 0.0
                sums33 += 0.0
                sums23 += 0.0
                sums13 += 0.0
                sums12 += 0.0

                sume11 += 0.0
                sume22 += 0.0
                sume33 += 0.0
                sume23 += 0.0
                sume13 += 0.0
                sume12 += 0.0
                sumivol += 0.0

                for j in range(0,len(S grout.values)):
```

```
                    ivol = IVOLgrout.values[j].data
                    s = Sgrout.values[j].data
                    e = Egrout.values[j].data

                    sums11 = s[0]ivol + sums11
                    sums22 = s[1]ivol + sums22
                    sums33 = s[2]ivol + sums33
                    sums23 = s[3]ivol + sums23
                    sums13 = s[4]ivol + sums13
                    sums12 = s[5]ivol + sums12

                    sume11 = e[0]ivol + sume11
                    sume22 = e[1]ivol + sume22
                    sume33 = e[2]ivol + sume33
                    sume23 = e[3]ivol + sume23
                    sume13 = e[4]ivol + sume13
                    sume12 = e[5]ivol + sume12

                    sumivol = ivol + sumivol



for adim in keys:
    step = odb.steps[adim]
    frameRepository = step.frames
    numFrames = len(frameRepository)
    for decre in range (numFrames,numFrames-1,  -1):
                grout instance = odb.rootAssembly.instances[ MATRIX-1 ]

                 for fr in range(0,decre):
                frame=step.frames[-1]

                S  = frame.fieldOutputs[ S ]
                E = frame.fieldOutputs[ E ]
                IVOL = frame.fieldOutputs[ IVOL ]
                Sgrout = S.getSubset(region=grout instance ,
                position=INTEGRATIONPOINT,
                elementType= C3D8 )
                Egrout = E.getSubset(region=grout instance ,
                position=INTEGRATIONPOINT,
```

```
                elementType= C3D8 )
                IVOLgrout = IVOL.getSubset(region=groutinstance,
                position=INTEGRATIONPOINT,
                elementType= C3D8 )


                for i in range(0,len(Sgrout.values)):
                    ivol = IVOLgrout.values[i].data
                    s = Sgrout.values[i].data
                    e = Egrout.values[i].data

                    sums111 += s[0]*ivol
                    sums221 += s[1]*ivol
                    sums331 += s[2]*ivol
                    sums231 += s[3]*ivol
                    sums131 += s[4]*ivol
                    sums121 += s[5]*ivol

                    sume111 += e[0]*ivol
                    sume221 += e[1]*ivol
                    sume331 += e[2]*ivol
                    sume231 += e[3]*ivol
                    sume131 += e[4]*ivol
                    sume121 += e[5]*ivol
                    sumivol1 += ivol


sumivol=sumivol+sumivol1
hs11=(sums111+sums11)/sumivol1
hs22=(sums221+sums22)/sumivol1
hs33=(sums331+sums33)/sumivol1
hs23=(sums231+sums23)/sumivol1
hs13=(sums131+sums13)/sumivol1
hs12=(sums121+sums12)/sumivol1

he11=(sume111 + sume11)/sumivol1
he22=(sume221 + sume22)/sumivol1
he33=(sume331 + sume33)/sumivol1
he23=(sume231 + sume23)/sumivol1
he13=(sume131 + sume13)/sumivol1
```

```
he12=(sume121 + sume12)/sumivol1

homogenizedstress = [hs11, hs22, hs33, hs23, hs13, hs12,sums111,sums11]
homogenizedstrain = [he11, he22, he33, he23, he13, he12,sume111,sume11]
ivols = [sumivol,sumivol,sumivol1]

print homogenizedstress
print homogenizedstrain
print ivols
print("     s seconds    "    (time.time()    starttime))
```

Listing B.2: Periodic boundary condition implementation on the surface nodes of the RVE written in Python

```
k=1    for set numbers of X
l=1    for constaint numbers of X
kk=1    for set numbers of Y
ll=1    for constaint numbers of Y
kkk=1    for set numbers of Z
lll=1    for constaint numbers of Z

  for x surfaces

for i in range(1,22):
    for j in range(1,22):

        mdb.models[ Model 1 ].rootAssembly.Set(name=( SetX  + str(k)), nodes=
            mdb.models[ Model 1 ].rootAssembly.instances[ matrix 1 ].nodes.
            getByBoundingSphere((1 ,1 0.1(j 1),2 0.1(i 1)),0.02))

        mdb.models[ Model 1 ].rootAssembly.Set(name=( SetX  + str(k+1)), nodes=
            mdb.models[ Model 1 ].rootAssembly.instances[ matrix 1 ].nodes.
            getByBoundingSphere(( 1 ,1 0.1(j 1),2 0.1(i 1)),0.02))

        mdb.models[ Model 1 ].Equation(name=( ConstraintXx  + str(l)),
        terms=(( 1.0, ( SetX  + str(k)), 1), (
            1.0, ( SetX  + str(k+1)), 1), (1.0,  SET RP 5 , 1)))

        mdb.models[ Model 1 ].Equation(name=( ConstraintXy  + str(l)),
        terms=(( 1.0, ( SetX  + str(k)), 2), (
            1.0, ( SetX  + str(k+1)), 2), (1.0,  SET RP 4 , 2)))

        mdb.models[ Model 1 ].Equation(name=( ConstraintXz  + str(l)),
        terms=(( 1.0, ( SetX  + str(k)), 3), (
            1.0, ( SetX  + str(k+1)), 3), (1.0,  SET RP 3 , 3)))
        l=l+1
        k=k+2

  for y surfaces

for ii in range(1,22):
    for jj in range (1,21):
```

```
        mdb.models[ Model 1 ].rootAssembly.Set(name=( SetY  + str(kk)), nodes=
            mdb.models[ Model 1 ].rootAssembly.instances[ matrix 1 ].nodes.
            getByBoundingSphere((0.9 0.1(jj 1),1,2 0.1(ii 1)),0.02))
        mm=kk+1
        mdb.models[ Model 1 ].rootAssembly.Set(name=( SetY  + str(mm)), nodes=
            mdb.models[ Model 1 ].rootAssembly.instances[ matrix 1 ].nodes.
            getByBoundingSphere((0.9 0.1(jj 1), 1,2 0.1(ii 1)),0.02))

        mdb.models[ Model 1 ].Equation(name=( ConstraintYx  + str(ll)),
        terms=(( 1.0, ( SetY  + str(kk)), 1), (
            1.0, ( SetY  + str(mm)), 1), (1.0,  SET RP 1  , 1)))

        mdb.models[ Model 1 ].Equation(name=( ConstraintYy  + str(ll)),
        terms=(( 1.0, ( SetY  + str(kk)), 2), (
            1.0, ( SetY  + str(mm)), 2), (1.0,  SET RP 2  , 2)))

        mdb.models[ Model 1 ].Equation(name=( ConstraintYz  + str(ll)),
        terms=(( 1.0, ( SetY  + str(kk)), 3), (
            1.0, ( SetY  + str(mm)), 3), (1.0,  SET RP 3  , 3)))
        ll+=1
        kk+=2

  for z surfaces

for iii in range(1,21):
    for jjj in range (1,21):

        mdb.models[ Model 1 ].rootAssembly.Set(name=( SetZ  + str(kkk)), nodes=
            mdb.models[ Model 1 ].rootAssembly.instances[ matrix 1 ].nodes.
            getByBoundingSphere((0.9 0.1(jjj 1),0.9 0.1(iii 1),2),0.02))
        mmm=kkk+1
        mdb.models[ Model 1 ].rootAssembly.Set(name=( SetZ  + str(mmm)), nodes=
            mdb.models[ Model 1 ].rootAssembly.instances[ matrix 1 ].nodes.
            getByBoundingSphere((0.9 0.1(jjj 1),0.9 0.1(iii 1),0),0.02))

        mdb.models[ Model 1 ].Equation(name=( ConstraintZx  + str(lll)),
        terms=(( 1.0, ( SetZ  + str(kkk)), 1), (
            1.0, ( SetZ  + str(mmm)), 1), (1.0,  SET RP 5  , 1)))
```

```
mdb.models[ Model 1 ].Equation(name=( ConstraintZy  + str(lll)),
terms=(( 1.0, ( SetZ  + str(kkk)), 2), (
    1.0, ( SetZ  + str(mmm)), 2), (1.0,  SET RP 2 , 2)))

mdb.models[ Model 1 ].Equation(name=( ConstraintZz  + str(lll)),
terms=(( 1.0, ( SetZ  + str(kkk)), 3), (
    1.0, ( SetZ  + str(mmm)), 3), (1.0,  SET RP 3 , 3)))
lll+=1
kkk+=2
```

Appendix C

In this section, the elasticity tensor is computed for the case with 290 randomly distributed particles without assuming any particular class of anisotropy. In other words, six different load cases are considered to determine all 36 constants of the elasticity tensor. The resultant elasticity tensor is given in Equation C.1.

$$\left[\ \boldsymbol{C}\ \right] = \begin{bmatrix} 1586.71 & 818.05 & 818.06 & 0.35 & 0.24 & 0.17 \\ 818.09 & 1577.17 & 817.17 & 0.06 & 0.07 & 0.05 \\ 818.09 & 817.17 & 1578.68 & 0.05 & 0.11 & 0.17 \\ 0.39 & 0.09 & 0.04 & 424.22 & 0.49 & 0.02 \\ 0.17 & 0.12 & 0.13 & 0.81 & 422.23 & 0.01 \\ 0.13 & 0.09 & 0.18 & 0.01 & 0.02 & 426.25 \end{bmatrix} \tag{C.1}$$

Equation C.1 shows that the response of the material is almost isotropic.